Alma Mater Studiorum · University of Bologna

School of Science
Department of Physics and Astronomy
Master Degree in Physics

Characterization of optic fiber for the LUCID-3 prototype during γ irradiation at Calliope facility at ENEA

Supervisor:
Prof. Maximiliano Sioli

Co-supervisor:
Dr. Federico Lasagni Manghi

Submitted by:
Davide Cremonini

Academic Year 2020/2021

Abstract

The luminosity is a fundamental running parameter for collider-based experiments since it is related to the cross section of every process and to the performance of the collider. Therefore its precise measurement is fundamental for every physics program. LUCID-2, the ATLAS main luminometer during Run-2, was able to measure luminosity with a precision of 1.7%. Similar performances are expected also for Run-3 but, starting from Run-4, the current design will not be able to satisfy all of the requirements foreseen by the ATLAS physics program. Therefore a new detector, called LUCID-3, must be built. There are several designs that can be grouped into two categories: fiber based detector and PMT-based detector. For testing purposes, 3 prototypes of LUCID-3 will be installed and tested during Run-3. One of these prototypes is a fiber based detector. For the correct operation of this prototype it is important to study how the fiber behaves when irradiated. Therefore a session of γ irradiation was performed at the Calliope facility at ENEA. To study how the light transmission changes as a function of the wavelength, various LEDs, going from UV to visible light, were used to inject light into the fibers during the irradiation. As expected, the largest signal losses were observed when using UV light. The relative losses, after an exposure of 705 kGy, were measured as 97%, 94%, 42%, 20% and 27% for deep UV (280 and 340 nm), UV (385 nm) and visible (476 and 525 nm) respectively.

Contents

List of Figures

List of Tables

Introduction

Luminosity is a fundamental parameter in accelerators physics because it is essential for the measurement of the cross section of every physics process and gives us information about the performance of the accelerator (LHC) in real time. Therefore, it's necessary to have a detector which is able to measure luminosity both online and offline with an high precision. LUCID-2 (LUminosity Cherenkov Integrating Detector) was the luminometer of the ATLAS Experiment for the Run-2 and guaranteed a precision in the luminosity measurement of 1.7%. A similar performance is expected for Run-3 but it cannot be obtained with the current detector at HL-LHC. Thus is necessary to build a new detector (LUCID-3) to guarantee an offline precision of 1% even in the prohibitive conditions of HL-LHC.

Many options for LUCID-3 have been developed and will be tested in Run-3. One of them is based on a FIBER detector. This detector will use new larger PMTs monitored by Bi-207, like LUCID-2, and a new type of radiation-hard fibers monitored by LED signals. The idea behind this detector is that a particle that passes through the fibers will emit Cherenkov light that goes to a PMT via the fibers themselves. Due to the high doses of radiation, we expect an opacification of the fibers that will lead to a greater loss of the Cherenkov light. The opacification depends on the wavelength so we expect a greater loss in the UV region than in the visible region.

To study this dependence, a session of gamma irradiation was performed using the Calliope facility at ENEA. This thesis reports the results and the experimental techniques used for the irradiation. An experimental system comprised of the fibers, LED's, power distribution and acquisition hardware and software was designed and tested pre-irradiation. Then the relevant data was acquired during the irradition: wavelelght-dependent light produced at the one end of the fibers and received at the opposite end. This data was then analysed to extract the fiber opacification as a function of the absorbed dose and of the injected light wavelength. From the literature a larger loss is expected in the deep UV range with a smaller loss in the visible or near-visible range of wavelengths.

Chapter 1

Beam Dynamics and Luminosity

1.1 Introduction

Although many topics would have a general validity, the main focus will be the ATLAS experiment at LHC at CERN, Geneva. Being a collider, in LHC there are 2 circulating beams rotating in opposite directions. Beams are divided into packets, called bunch, since the accelerator system (that will be explained later) is not able to accelerate continuous beams. This meas that the collisions will happen only in certain time frames called BCID (Bunch crossing ID). Although the beam can be made by ions, in this thesis we will consider only proton beams since the ATLAS experiment works with proton beams.

1.2 Beam dynamics

To describe properly the concept of luminosity for a collider and the techniques for its measurement is necessary to study the dynamic of a beam.

1.2.1 Electric and Magnetic Fields

A charged particle, in the electromagnetic field of an accelerator, gains energy by the interaction with the electric field $\vec{E}$ and its trajectory is curved when it passes through a dipole magnet. At relativistic velocities, an electric field $\vec{E}$ and a magnetic field $\vec{B}$ have the same effect: a magnetic field of 1 T would be, at this condition, equal to an electric one of $3 \cdot 10^8 \mathrm{V} \cdot \mathrm{m}^{-1}$. The effects of a magnetic field are first analyzed and then the effects of the electric one.

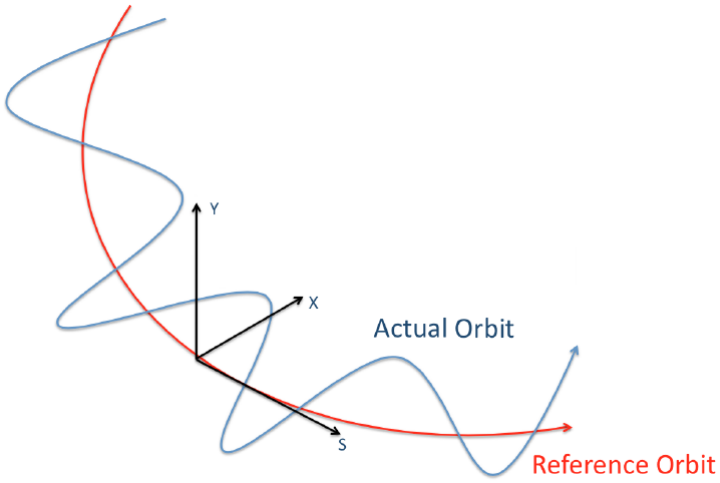

Figure 1.1: Beam dynamics scheme. The reference orbit is drawn in red while the effective orbit is drawn in blue.

A typical coordinate system (x, y, s) used to describe the particle's motion is shown in Fig. 1.1. In order to describe the path of the particles, s is the longitudinal direction along the reference orbit, while x and y are the transversal coordinates which define the transverse plane. We call $\vec{r_0}$ the reference trajectory with null x and y coordinates for every s. The particle trajectory around the reference orbit can be expressed as:

$$\vec{r} = \vec{r_0} + x\hat{x}(s) + y\hat{y}(s) \tag{1.1}$$

The $\vec{B}$ field components can be expressed as a function of a dipolar and quadrupolar term. Dipole magnets guide the charged particles along the closed orbit and the Lorentz force bends the trajectory with a bending angle θ

$$\theta = \frac{q}{p}\int_{s_1}^{s_2} Bdl = \frac{1}{B\rho}\int_{s_1}^{s_2} Bdl \tag{1.2}$$

where p and q are the momentum and the charge of the particle, respectively, while ρ is the bending radius. Knowing that the total bending angle of a circular accelerator is 2π, the total dipole field is

$$\oint Bdl = \frac{2\pi p}{q} = 2\pi B\rho \tag{1.3}$$

from which we obtain the bending radius ρ

$$\rho = \frac{mv}{qB} = \frac{p}{qB}. \tag{1.4}$$

While dipole magnets are used to bend the particle's trajectory, quadrupole magnets are used to focus or defocus the beam and to control the beam size. A focusing quadrupole in the horizontal plane corresponds to a defocusing one on the vertical plane and viceversa.

The task of the electric fields is to accelerate the charged particles. There are various technologies that can be used and the choice depends on the scale of energy. At high energies, radio frequencies (RF) are used to generate a longitudinal electric field. The passage through a RF cavity induce a variation of energy of $\Delta E = q\Delta V$ where $\Delta V = V_0 \sin(\omega_{RF} t + \phi)$ is the effective gap voltage, ω_{RF} is the RF frequency, V_0 is the effective peak accelerating voltage and ϕ is a phase. To be properly accelerated, particles must be in phase with the accelerating voltage. Thus, the RF frequency must be an integer (h) multiple of the revolution frequency. In that way, the particle crosses the electric field every turn at a constant phase and so experiences a constant force.

$$f_{RF} = h \cdot F_{rev}. \tag{1.5}$$

A particle with a speed β (in units of c) circulates in the accelerator with a period $T_{rev} = \frac{2\pi R}{\beta c}$ and a frequency $f_{rev} = \frac{\beta c}{2\pi R}$ (in LHC, $f_{rev} = 11KHz$).

1.2.2 Betatron Motion and Transverse Emittance

The betatron motion describes the motion of the particle in the transverse plane, around the reference orbit. The equation describing this motion is derived from the Lorentz force. Knowing that $\vec{B}$ is non-null only on the transverse plane xy, the Hill's equations [2] can be written as:

$$x'' + K_x(s)x = 0 \tag{1.6}$$

$$y'' + K_y(s)y = 0 \tag{1.7}$$

$$K_x = \frac{1}{\rho^2} \mp K_1(s) \tag{1.8}$$

$$K_y = \mp K_1(s) \tag{1.9}$$

where $K_1(s) = \frac{B_1(s)}{B\rho}$ is the effective focusing function which sign depends on the charge of the particle and $B_1(s)$ is the magnetic field evaluated at the center of the quadrupole. $K_x(s)$ and $K_y(s)$ are periodic function and can be assumed constant because in the accelerator magnetic field components are nearly uniform.

Considering only the y axis and imposing the periodic condition $K(s + L) = K(s)$, where L is the distance between two successive quadrupole stations, the solution to Hill's equation can be written as:

$$y(s) = \begin{cases} A\cos(\sqrt{K}s + b) & \text{per} K > 0 \\ As + b & \text{per} K = 0 \\ A\cosh(\sqrt{-K}s + b) & \text{per} K < 0 \end{cases} \tag{1.10}$$

An alternative expression can be expanded in terms of the betatron state vector and the betatron transfer matrix M[1]:

$$\mathbf{y}(s) = \begin{pmatrix} y(s) \\ y'(s) \end{pmatrix} \tag{1.11}$$

$$\mathbf{y}(s) = M(s|s_0)y(s_0) \tag{1.12}$$

Eq 1.12 is the solution of the Hills equations as a function of the betatron sate vector and the transfer matrix, where $M(s|s_0)$ has the following expression, depending on $K(l = s - s_0)$ and in the case of $K > 0$ (focusing quadrupole):

$$M = \begin{pmatrix} \cos\sqrt{|K|}l & \frac{1}{\sqrt{k}}\sin\sqrt{K}l \\ -\sqrt{K}\sin\sqrt{K}l & \cos\sqrt{|K|}l \end{pmatrix} \tag{1.13}$$

The previous equation can be rewritten in the following way:

$$y(s) = A\omega(s)\cos(\Phi(s) - \Phi_0) \tag{1.14}$$

where $\omega(s)$ is a periodic function with periodicity L, $\Phi(s) = \sqrt{K}s$, A and Φ_0 are the integration constants. Since $K(s)$ is a periodic function, $K(s + L) = K(s)$ where the period L can coincide with the accelerator circumference but usually corresponds to the distance between two consecutive quadrupoles. From equation 1.14 we can define a new set of variables, called Courant-Snyder functions or Twiss parameters:

$$\beta(s) = \frac{\omega^2(s)}{K} \tag{1.15}$$

$$\alpha(s) = -\frac{1}{2}\frac{\partial\beta(s)}{\partial s} \tag{1.16}$$

$$\gamma(s) = \frac{1 + \alpha^2(s)}{\beta(s)}. \tag{1.17}$$

$\beta(s)$ is also called betatron amplitude function. Using eqs. 1.15, 1.16 and 1.17 we can parametrize the transfer matrix that describes a complete turn around the ring as

$$\mathbf{M} = \begin{pmatrix} \cos\Phi + \alpha\sin\Phi & \beta\sin\Phi \\ -\gamma\sin\Phi & \cos\Phi - \alpha\sin\Phi \end{pmatrix} \tag{1.18}$$

where Φ is the betatron phase advance, defined as:

$$\Phi = \int_{s_0}^{s_0+L} \frac{ds}{\beta(s)} \tag{1.19}$$

where L is the length of the periodic beam line for which the K function is periodic. For an accelerator of circumference $C = NL$ with N identical superperiods, $N\Phi$ is the phase change per revolution. We can also derive two characteristic quantities, Q_x and Q_y, called betatron tunes which indicates the number of betatron oscillation per revolution

$$Q_i = \frac{N\Phi_i}{2\pi} = \frac{1}{2\pi}\int_s^{s+C} \frac{ds}{\beta_i(s)} \tag{1.20}$$

where $i = x, y$. The betatron oscillation frequency is given by $Q_i f_0$, where f_0 is the revolution frequency. The general solution of the Hills equations along the y-axis can be written as

$$y(s) = a\sqrt{\beta_y(s)}\cos[\Phi_y(s) + \Phi_0] \tag{1.21}$$

where

$$\Phi_y(s) = \int_0^s \frac{ds}{\beta_y(s)} \tag{1.22}$$

. Therefore, we will have pseudo-harmonic oscillation with variable amplitude of $\sqrt{\beta_y(s)}$.

1.2.3 Beam Emittance

The particle distribution is generally described by a six dimensional density function ρ in which x, y and s represent the variables that define the coordinate system. In linear dynamics the transverse and longitudinal distributions are often considered as uncorrelated, so the six dimension can therefore be factorized into three independent phase-space (x, x') (y, y') and (s, E).

Replacing $\Phi_y(s) + \Phi_0$ by $\theta(s)$ in Eq. 1.21 we obtain

$$y(s) = a\sqrt{\beta_y(s)}\cos\theta(s) \tag{1.23}$$

and deriving

$$y'(s) = -\frac{a}{\sqrt{\beta_y(s)}}[\sin\theta(s) + \alpha(s)\cos\theta(s)]. \tag{1.24}$$

Combining both of them together we obtain the following equation

$$\gamma y^2 + 2\alpha y y' + \beta y'^2 = a^2 \tag{1.25}$$

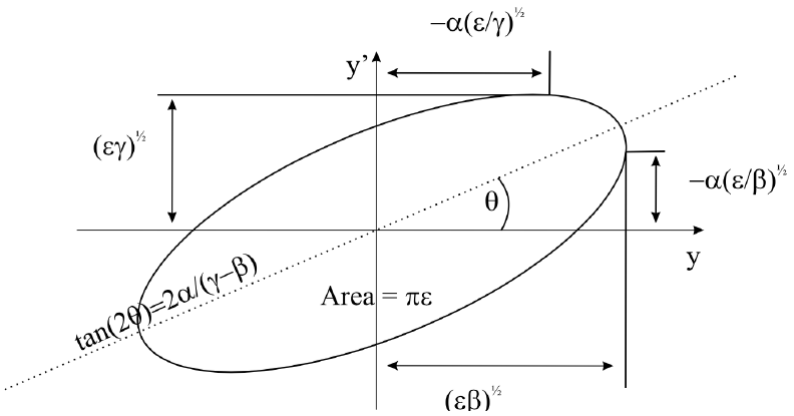

Figure 1.2: Scheme of the motion of the particle in the phase space. Typically, it can be represented as an ellipse parametrized through Courant-Snyder parameters.

which is the Courant-Snyder invariant which remains constant along a particle trajectory and describes an ellipse (Fig 1.2), in the phase-space (y, y'). a^2 is called emittance of a single particle following its individual trajectory:

$$\epsilon = a^2 = \frac{Ellipse\,area}{\pi}. \tag{1.26}$$

The emittance is the area of the ellipse which contains a certain percentage of particles.

A beam is composed by particles centered around the reference orbit, so for any distribution of particles, it's possible to define a region in phase space occupied by all of them. Taking a normalized distribution function $\rho(y, y')$, the moments of the beam distribution are

$$\langle y \rangle = \int\int y\,\rho(y, y')\,dydy' \tag{1.27}$$

$$\langle y' \rangle = \int\int y'\,\rho(y, y')\,dydy' \tag{1.28}$$

$$\sigma_y^2 = \int\int (y - \langle y \rangle)^2 \rho(y, y')\,dydy' \tag{1.29}$$

$$\sigma_{y'}^2 = \int\int (y' - \langle y' \rangle)^2 \rho(y, y')\,dydy' \tag{1.30}$$

$$\sigma_{yy'} = \int\int (y - \langle y \rangle)(y' - \langle y' \rangle)\rho(y, y')\,dydy' = r\sigma_y\sigma_{y'} \tag{1.31}$$

where σ_y and $\sigma_{y'}$ are the RMS beam widths, $\sigma_{yy'}$ is the correlation and r is the correlation coefficient.

The RMS beam emittance is defined as:

$$\epsilon_{rms} = \sqrt{\sigma_y^2\sigma_{y'}^2 - \sigma_{yy'}^2} = \sigma_y\sigma_{y'}\sqrt{1 - r^2} \tag{1.32}$$

and it is equal to the phase space area enclosed by the Courant-Snyder ellipse of the RMS particle. It can be shown that for a beam with RMS emittance $\pi\epsilon$, the RMS beam width is

$$\sigma_y = \sqrt{\beta\epsilon}. \tag{1.33}$$

1.3 Luminosity

From a physical point of view, luminosity $\mathcal{L}$[3][4] is defined via the following formula:

$$\mathcal{L} = \frac{R}{\sigma} \tag{1.34}$$

where R is the rate of a generic physical process while σ is its cross section. A precise absolute luminosity measurement is necessary for every cross section measurement, although the required precision can vary from analysis to analysis.

We can define two different types of luminosities:

- the instantaneous luminosity $\mathcal{L}$, defined by the previous formula, is related to the instantaneous performance of the collider, may fluctuate on time scales from tens of nanoseconds to minutes, and typically decays with time constants of hours or even days.
- the integrated luminosity, denoted by $\int \mathcal{L}dt$ refers to the instantaneous luminosity accumulated over a certain time interval and is typically quoted in units of cm^{-2}, or equivalently in inverse barns, microbarns (μb^{-1}), picobarns (pb^{-1}), etc.

The experimental technique implemented at LHC to measure both the integrated and the instantaneous luminosity are described in the following sections. These Techniques can be divided in direct and indirect. In direct measurements, such as the so-called Van der Meer scans or the beam gas interaction scans, the absolute luminosity is inferred from bunch properties. In indirect measurements, information on physics processes like measured rates are used. The measured rate is in fact only proportional to the absolute luminosity and it is referred to as relative luminosity.

Both relative and absolute luminosity are important: the first one because it is used to grant a correct measurement of the integrated luminosity, the second one because affects directly cross section measurements. Moreover, in luminosity-based accelerators, the relative luminosity is used to evaluate online the performance of the machine in real time and to tune its parameters.

1.4 Luminosity from Beam Parameters

The absolute luminosity can be obtained starting from the parameters of the accelerator. For simplicity, we make some assumption on the beams and on the collisions[5]:

- the transverse and longitudinal beam densities are Gaussian;
- linear x–y coupling is small enough to be neglected
- dispersion at interaction point (IP) and angular dispersion are negligible;
- beam–beam-induced effects are negligible.

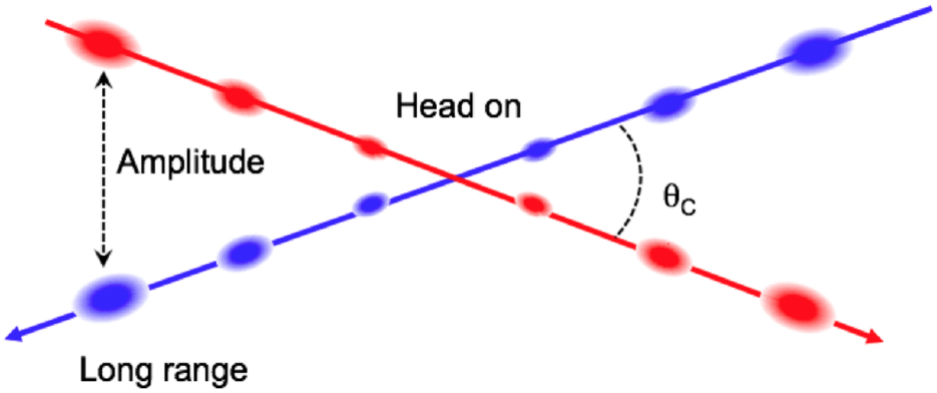

Figure 1.3: Scheme of the collision between 2 bunches with a non-zero crossing angle(θ_c).

The bunch luminosity $\mathcal{L}_b$ produced by one colliding-bunch pair (Fig. 1.3), with time- and position-dependent density functions $\rho_1(x, y, z, t)$ and $\rho_2(x, y, z, t)$ is given by:

$$L_b = f_r n_1 n_2 K \int \rho_1(x, y, z, t)\rho_2(x, y, z, t)\, dx\, dy\, dz\, dt \tag{1.35}$$

where 1 refers to bunch 1 and 2 refers to bunch 2, f_r is the revolution frequency, n_1 and n_2 are the number of protons in each bunch and the densities are normalized such that their spatial integral is equal to 1 for each time. The kinematic factor K is given by

$$K = \sqrt{(\vec{v_1} - \vec{v_2})^2 - \frac{(\vec{v_1} \times \vec{v_2})^2}{c^2}} \tag{1.36}$$

where $\vec{v_1}$ and $\vec{v_2}$ are the velocities of each beam. Supposing that $\vec{v_1}$ and $\vec{v_2}$ have the same module, the lab frame is defined in the following way: x-axis points in the direction of $\vec{v_1} + \vec{v_2}$, y-axis in that of $\vec{v_1} \times \vec{v_2}$ and the z-axis is parallel to $\vec{v_1} - \vec{v_2}$. The crossing angle lies in the xz plane.

Assuming that $v_1 = v_2 = c$, the bunch luminosity simplifies to

$$L_b = f_r\, n_1\, n_2\, 2c \cos\theta_c \int \rho_1(x, y, z, t)\rho_2(x, y, z, t)\, dx\, dy\, dz\, dt \tag{1.37}$$

The beam density is defined

$$\rho_B = \frac{1}{\sqrt{(2\pi)^3}\sigma_{xB}\sigma_{yB}\sigma_{zB}} \times exp\left[-\frac{(x-x_B)^2}{2\sigma_{xB}^2} - \frac{(y-y_B)^2}{2\sigma_{yB}^2} - \frac{(z-ct)^2}{2\sigma_{zB}^2}\right] \tag{1.38}$$

where $B = 1, 2$ indicates the two beams, σ_{jB} $(j = x, y, z)$ is the dimension of the beam. If the crossing angle is null the bunch luminosity becomes

$$L_b = f_r\, n_1\, n_2\, 2c \int \rho_1(x, y, z, t)\rho_2(x, y, z, t)\, dx\, dy\, dz\, dt = \frac{f_r\, n_1\, n_2}{2\pi\, \Sigma_x\, \Sigma_y} \tag{1.39}$$

where

$$\Sigma_j = \sqrt{\sigma_{j1}^2 + \sigma_{j2}^2}.$$

If the two beams have the same dimensions ($\sigma_{x1} = \sigma_{x2}$ and $\sigma_{y1} = \sigma_{y2}$) $\mathcal{L}_b$ can thus rewritten as

$$L_b = \frac{f_r\, n_1\, n_2}{4\pi\, \sigma_x\, \sigma_y} \tag{1.40}$$

If in addition $\epsilon_x = \epsilon_y$ and $\beta_x^* = \beta_y^*$, then the means are round ($\sigma_x = \sigma_y$) and

$$L_b = \frac{f_r\, n_1\, n_2}{4\pi\, \sigma^2} = \frac{f_r\, n_1\, n_2\, \gamma}{4\pi\, \epsilon_N\, \beta^*} \tag{1.41}$$

where $\epsilon_N = \gamma\, \beta\, \epsilon$ is called the normalized emittance, γ is the relativistic Lorentz factor and β is the velocity. The total instantaneous luminosity is given by

$$\mathcal{L} = \sum_b \mathcal{L}_b \tag{1.42}$$

Some effects that reduce the luminosity as defined so far: crossing angle, offset collision and hourglass effect. These will be discussed in the following paragraphs. Other effects that have an impact on the maximum obtainable luminosity are related to dispersion effects and beam-beam interactions. The analysis of these effects is outside the scope of this thesis and therefore won't be treated

1.4.1 Crossing Angle

The crossing angle is introduced in order to restrict collisions only to the IP and to avoid unwanted parasitic-collisions at the other positions in the ring where the two beams are not separated. Due to the crossing angle θ_c, the luminosity is reduced by a factor:

$$F_c = \sqrt{1 + \left(\frac{\theta_c \sigma_s}{2\theta^*}\right)^2} \tag{1.43}$$

where σ_s is the longitudinal (s) bunch length and σ^* the transverse R.M.S. beam size at the interaction point.

1.4.2 Offset Collisions

The two beams do not always collide head-on, actually they can be shifted in the horizontal and vertical directions by arbitrary displacements x_i and y_i $(i = 1, 2)$. The beam density has to be rewritten in the following way:

$$\rho_i = \frac{1}{\sigma_{ix}\sqrt{2\pi}} e^{-\left(\frac{(x-x_i)^2}{2\sigma_{ix}^2}\right)} \tag{1.44}$$

$$\rho_i = \frac{1}{\sigma_{iy}\sqrt{2\pi}} e^{-\left(\frac{(y-y_i)^2}{2\sigma_{iy}^2}\right)} \tag{1.45}$$

The luminosity will be

$$\mathcal{L} = \mathcal{L}_{MAX} e^{\left[-\frac{(\delta_x)^2}{2(\sigma_{1x}^2+\sigma_{2x}^2)} - \frac{(\delta_y)^2}{2(\sigma_{1y}^2+\sigma_{2y}^2)}\right]} \tag{1.46}$$

where $\mathcal{L}_{MAX}$ is the luminosity in head-on collision case and δ_x and δ_y represent the two displacements of the centroids in the transverse plane.

1.4.3 Hourglass Effect

The beam size $\sigma(s)$ is related to the betatron function and emittance:

$$\sigma(s) = \sqrt{\epsilon\beta(s)}. \tag{1.47}$$

At the interaction point, $\beta(s)$ is typically adjusted to have a local minimum in order to minimize the beam size and consequently maximize the interaction rate. The value of $\beta(s)$ at the IP is known as β^*.

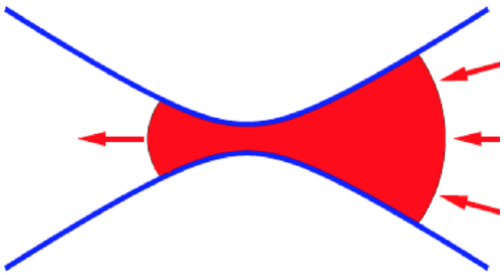

Figure 1.4: Pictorial view of Hourglass Effect. The bunch shape at the IP is drawn in red and the blue line indicates the parabolic shape of the β function. The bunch has a minimum in transverse size at the IP and grows moving away from it.

The assumption of the previous discussion is that the beam density functions are uncorrelated in the transverse and longitudinal planes and that the beam sizes are constant in the collision region. Actually, for low β^*, this is not a good approximation. The β-function varies around the minimum value as:

$$\beta(s) = \beta^* \left(1 + \frac{s^2}{\beta^{*2}}\right) \tag{1.48}$$

and the transverse beam size $\sigma(s)$ will be:

$$\sigma(s) = \sigma^* \sqrt{1 + \frac{s^2}{\beta^{*2}}} \tag{1.49}$$

The effect is known as hourglass effect because of the shape of the function (Fig. 1.4). The maximum luminosity is obtained for collisions occurring exactly at the IP, while away from the IP the beam size increases and the luminosity decreases. This effect becomes relevant if β^* is small compared to the bunch length, in particular if the ratio $r = \frac{\beta^*}{\sigma_s} \approx 1$.

1.5 Relative-luminosity Monitoring Methods

The bunch luminosity can be written as[6]:

$$L_b = \frac{R_{ref,b}}{\sigma_{ref}} \tag{1.50}$$

where $R_{ref,b}$ is the rate of a reference collision process in a bunch crossing and σ_{ref} is the corresponding cross-section. The reference process can in principle be chosen arbitrarily; choosing inelastic *pp* collisions as a typical one, the above equation can be rewritten as

$$L_b = \frac{\mu_b f_r}{\sigma_{inel}} \tag{1.51}$$

where μ_b is the average number of inelastic interactions per bunch crossing (BC), also called pile-up parameter, f_r is the bunch revolution frequency, and σ_{inel} is the inelastic pp cross-section. There are various techniques for luminosity measurement but can be classified in 3 different categories[7]:

- *Event counting:* the fraction of bunch crossings during which a specified detector registers an "event" satisfying a given selection requirement is counted. For instance, a bunch crossing can be said to contain an "event" if at least one *pp* interaction in that crossing induces at least one observed hit in the detector being considered.

- *Hit counting:* the number of hits (for example the number of electronic channels or energy clusters above a specified threshold) per bunch crossing in a given detector is counted

- *Particle counting:* luminosity is proportional the distribution of the number of particles per beam crossing (or its mean) inferred from reconstructed quantities such as calorimeter-energy distributions, or from other observables that reflect the instantaneous particle flux traversing the detector

Eq. (1.51) can be rewritten as:

$$L_b = \frac{\mu_b f_r}{\sigma_{inel}} = \frac{\mu_{vis} f_r}{\epsilon \sigma_{inel}} = \frac{\mu_{vis} f_r}{\sigma_{vis}} \tag{1.52}$$

where ϵ is the efficiency for one inelastic *pp* collision to satisfy the event-selection criteria, and $\mu_{vis} = \epsilon\mu$ is the average number of visible inelastic interactions per BC. The visible cross-section $\sigma_{vis} = \epsilon\sigma_{inel}$ is the calibration constant that relates the measurable quantity μ_{vis} to the absolute bunch luminosity $\mathcal{L}_b$.

If the probability of more than one interaction to occur within a bunch crossing is low enough, the relative luminosity can be monitored simply using an arbitrary physics process with sufficiently high rate and low enough background:

$$L_b = \frac{R_{vis}}{\sigma_{vis}} \tag{1.53}$$

In this case, the mean number of visible interaction is:

$$\mu_{vis} = \frac{N}{N_{BC}} \tag{1.54}$$

where N is is the (background-subtracted) number of events passing the selection criteria that are observed during a given time interval, and N_{BC} the number of bunch crossings in that same interval. When μ increases, the probability that two or more *pp* interactions occur in the same bunch crossing is no longer negligible, and μ_{vis} is no longer linearly related to the raw event count N. Instead μ_{vis} must be calculated taking into account Poisson statistics and instrumental or pile-up-related effects.

1.5.1 Event counting

In order to determine the value of μ_{vis} some assumptions are made:

- the number of pp interactions follows the Poisson statistics;

- the efficiency to detect a single inelastic *pp* interaction is constant, in the sense that it does not change when several interactions occur in the same bunch crossing. This is equivalent to assuming that the efficiency ϵ_n for detecting one event associated with n interactions occurring in the same crossing is given by

$$\epsilon_n = 1 - (1 - \epsilon_1)^n \tag{1.55}$$

  where ϵ_1 is the detection efficiency corresponding to a single inelastic interaction in a bunch crossing.

Thus, the absolute bunch luminosity is given by:

$$L_b = \frac{\mu_{vis} f_r}{\sigma_{vis}} \tag{1.56}$$

using the value of σ_{vis} measured, for instance, by the van der Meer method. To measure the value of μ_{vis} different algorithms like OR-algorithm and AND-algorithm can be used.

OR-algorithm

LUCID, like many others luminometers in ATLAS, is made of 2 symmetrical elements with respect to the interaction point (IP) called side-A and side-C. In an Event-OR algorithm, a bunch crossing is counted as containing an "event" if there is at least one hit on either the A or the C side of the detector. Since the Poisson probability for observing zero events in a given bunch crossing is $P_0(\mu_{vis}) = e^{-\mu_{vis}} = e^{-\mu\epsilon^{OR}}$, the probability of observing at least one event is

$$P_{OR}(\mu_{vis}) = \frac{N_{OR}}{N_{BC}} = 1 - P_0 = 1 - e^{-\mu_{vis}} \tag{1.57}$$

where N_{OR} is the number of bunch in which happened at least one interaction that satisfies the selection criteria and N_{OR} is the total number of colliding bunch. Solving for μ_{vis}:

$$\mu_{vis} = -\ln\left(1 - \frac{N_{OR}}{N_{BC}}\right) \tag{1.58}$$

AND-algorithm

In this case, a bunch crossing is counted if there is at least one hit in each of the two detector arms. This coincidence condition can be satisfied either from a single *pp* interaction or from individual hits on either side of the detector from different *pp* interactions in the same bunch crossing. Therefore, the event-counting probability no longer depends on a single efficiency: it must be written in terms of ϵ^A, ϵ^C and ϵ^{AND},

the efficiencies for observing an event with, respectively, at least one hit on the A-side, at least one hit on the C-side and at least one hit on both sides simultaneously.

The probability $P_{AND}(\mu)$ of there being at least one hit on both sides is one minus the probability $P_0^{Zero_{OR}}$ of there being no hit on at least one side. The latter, in turn, equals the probability that there be no hit on at least side A($P_{0A} = e^{-\mu\epsilon^A}$), plus the probability that there be no hit on at least side C($P_{0C} = e^{-\mu\epsilon^C}$), minus the probability that there be no hit on either side($P_0 = e^{-\mu\epsilon^{OR}}$):

$$\begin{aligned} P_{AND}(\mu) = \frac{N_{AND}}{N_{BC}} &= 1 - P_0^{Zero_OR} \\ &= 1 - (e^{-\mu\epsilon^A} + e^{-\mu\epsilon^C} + e^{-\mu\epsilon^{OR}}) \\ &= 1 - e^{-\mu\epsilon^A} - e^{-\mu\epsilon^C} - e^{-\mu\epsilon^{OR}} \end{aligned} \tag{1.59}$$

This equation cannot be inverted analytically, and the best approach depends on the values of ϵ^A, ϵ^C and ϵ^{AND}.

If the layouts, geometries and efficiencies of the forward and backward luminometers are sufficiently similar, the above equation can be simplified under the assumption that $\epsilon^A \approx \epsilon^C$. The efficiencies ϵ^{AND} and ϵ^{OR} are defined as, respectively, $\epsilon^{AND} \equiv \sigma_{vis}^{AND}/\sigma_{inel}$ and $\epsilon^{OR} \equiv \sigma_{vis}^{OR}/\sigma_{inel}$. The average number of visible inelastic interactions per BC is computed as $\mu_{vis} \equiv \epsilon^{AND}\mu$. The previous equation can be thus rewritten as:

$$\begin{aligned} \frac{N_{AND}}{N_{BC}} &= 1 - 2e^{-\mu(\epsilon^{AND}+\epsilon^{OR})} + e^{-\mu\epsilon^{OR}} \\ &= 1 - 2e^{-\mu_{vis}(\sigma_{vis}^{AND}/\sigma_{inel}+\sigma_{vis}^{OR}/\sigma_{inel})/2} + e^{-\mu_{vis}\sigma_{vis}^{OR}/\sigma_{inel}} \end{aligned} \tag{1.60}$$

If the efficiency is high and $\epsilon^{AND} \approx \epsilon^A \approx \epsilon^C$, Eq.(1.59) can be approximated by

$$\mu_{vis} \approx -ln\left(1 - \frac{N_{AND}}{N_{BC}}\right) \tag{1.61}$$

1.5.2 Hit counting

When $\mu_{vis} \gg 1$, event-counting algorithms lose sensitivity as fewer and fewer bunch crossings in a given time interval report zero observed interactions: this is known as saturation or zero starvation. In the limit where $N/N_{BC} = 1$, it is no longer possible to use event counting to determine the interaction rate μ_{vis}, and more sophisticated techniques must be used. One example is hit counting, where the number of hits in a given detector is counted rather than just the total number of events. This provides more information about the interaction rate per event, and raises the luminosity at which the algorithm saturates.

Under the assumption that the number of hits in one *pp* interaction follows a binomial distribution[1] and that the number of interactions per bunch crossing follows a Poisson distribution, the average probability to have a hit per bunch crossing in one of the detector channels can be calculated as

$$P_{HIT}(\mu_{vis}^{HIT}) = \frac{N_{HIT}}{N_{BC}N_{CH}} = 1 - e^{\mu_{vis}^{HIT}} \tag{1.62}$$

where N_{HIT} is the total numbers of hits, N_{BC} is the total numbers of bunch crossings and N_{CH} is the number of detector channels. μ_{vis}^{HIT} can be calculate as:

$$\mu_{vis}^{HIT} = -ln\left(1 - \frac{N_{HIT}}{N_{BC}N_{CH}}\right) \tag{1.63}$$

Therefore, the bunch luminosity becomes

$$L_b = \frac{\mu_{vis}^{HIT} f_r}{\sigma_{vis}^{HIT}} \tag{1.64}$$

Hit-counting algorithms are typically more sensitive than event-counting methods to instrumental imperfections such as threshold effects, instrumental noise, channel-to-channel efficiency variations and long-term gain drifts. Even so, such algorithms have been used successfully in the hostile experimental environment of the LHC, where very high values of the pile-up parameter μ render event counting impractical for large-acceptance luminometers.

Pile-up Effects and Non-Linearity

The applicability of the Poisson formalism depends on the validity of the assumption expressed by Eq.1.55: the efficiency for detecting an elastic *pp* interaction is independent of the number of interactions that occur in each bunch crossing or equivalently, from the detector's point of view, the interactions are independent of each other. This latter assumption is intrinsically not true when a threshold is set to define a hit (and consequently an event), which is exactly the way event and hit counting work. If, for example, two *pp* interactions happen in the same bunch crossing, both producing signals in the detector which are individually below the threshold (i.e. they would not be individually detected), but whose sum is above the threshold, then this assumption is clearly violated. The same holds if background not related to the *pp* interaction add up to produce a hit in addition or even without signals from collisions. The result is that the Poisson assumption is violated and non-linearities appear in the luminosity measurement with increasing pile-up. This effect is called migration and can be reduced, but

[1] This is true only if the probability to register a signal is independent on the number of signals in the other channels

not eliminated, by lowering as much as possible the thresholds. Only in the impossible limit of zero-threshold, the effect disappears. Migration becomes more important as the pile-up parameter increases.

1.5.3 Particle Counting

The advent of large-acceptance, high-precision silicon trackers at the LHC has enabled the development of additional algorithms that are based on reconstructing charged-particle tracks and from these, *pp* interaction vertices.

Track-based event counting consists in measuring the fraction of bunch crossings with a minimum number of tracks (typically 1 or 2) reconstructed in the silicon trackers. Track counting is conceptually similar to hit counting and is in some respects more robust, e.g. for what regards background subtraction. It amounts to counting the number of well-reconstructed tracks per bunch crossing, with the track quality ensured by tight selection criteria.

In vertex-counting algorithms, the average number of visible interactions per bunch crossing is determined by counting the number of reconstructed vertices found in each bunch crossing. In its principle, the method is intrinsically linear and is applicable to much higher μ regimes than vertex-based event counting. But it suffers from nonlinear behavior with increasing pile-up parameter, primarily due to two effects: vertex masking and fake vertices.

1.6 Absolute luminosity calibration

To measure luminosity starting from μ_{vis} is necessary to calibrate detectors and algorithms determining the visible cross section σ_{vis}[8].

The simplest method is to compare the visible interaction rate μ_{vis} to the absolute luminosity computed, in the same time interval, with measured beam parameters. For example, far from the IP, the parameters of the two beams can be separately estimated and then extrapolated to the collision point. Unfortunately this technique has a limited precision. A more accurate technique is the determination of the beam-overlap area directly at the IP using the beam-separation scans. A different approach is to measure, in dedicated runs, the elastic *pp* cross section at small angle and, using the optical theorem, to extract both the total cross section and the luminosity and relate it with the rate measured by the luminosity detectors. Finally well known physics processes for which not only the cross section, but also the total acceptance and efficiency are known with sufficient precision can be used. In the following paragraphs will be discussed only the first two methods since they are both used by the ATLAS experiment.

1.6.1 Measurement of Beam Parameters

The bunch luminosity (eqs 1.39, 1.40) can be calculated from the population of the two bunches n_B and from their transversal section σ_{iB} (i=x,y; B=1,2). Although the measurement of the population has reached a precision of 1%, a precise measurement of the transversal section of the bunches at IP is very difficult due to the experimental resolution and spatial limitations. The beam-profile monitoring is based on wire scanners or synchrotron light telescope methods. The monitors are installed in diagnostic regions away from the IP and they usually reports the projected horizontal and vertical RMS beam sizes, which can be extrapolated to the interaction point using an optical model of the collider lattice. Nevertheless, this technique has some limitation to be taken into account.

- Instrumental systematics (such as wire scanning speed, beam-induced heating, distortion of optical mirrors, resolution effects, etc.) make the precise determination of the absolute transverse beam size at the monitor rather challenging.
- The determination of the single-beam sizes to the IP requires the knowledge of a certain set of parameters, such as the betatron functions and betatron phases, both at the monitor points and at the IP. These parameters must be determined in separated sessions and their combination typically contribute with significant amount to the uncertainty to each of the four IP single-beam sizes σ_{iB}.
- Extrapolation becomes challenging when transverse coupling, dispersion and dynamic-β effects play a significant role.
- The assumption of Gaussian beams, factorisable in x and y, may demonstrate itself as an incorrect hypothesis, because of instrumental limitations.

Typical precisions obtained with such methods are not better than 10-15%.

1.6.2 Van der Meer Scan

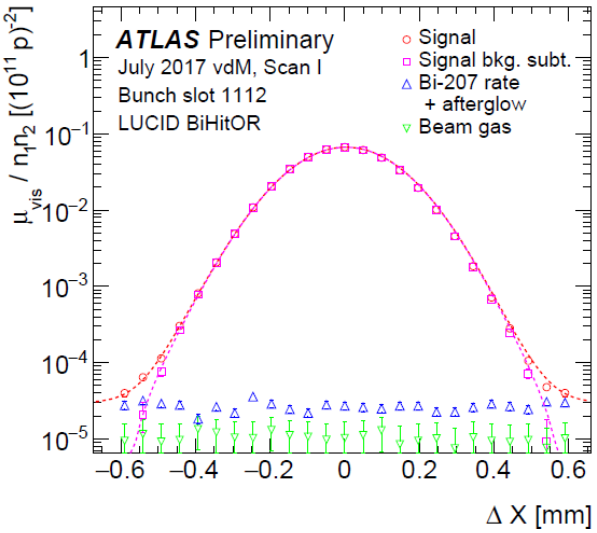

Figure 1.5: Visible interaction rate per unit bunch population vs beam separation as measured by LUCID for bunch 1112 in scan 1 of the July 2017 VdM session

At LHC, the primary technique to determine the absolute luminosity scale is based on dedicated beam-separation scans, whereby the absolute luminosity is inferred, at one point in time, from the measurable parameters of the colliding bunches. By comparing the known luminosity delivered at the peak of the Van der Meer (VdM)[9] (fig 1.5) scan to the visible interaction rate μ_{vis}, the visible cross-section of inelastic pp collisions can be determined. To achieve the desired accuracy on the absolute luminosity, these scans are usually performed not during normal physics operations, but under carefully controlled conditions and with beam parameters optimized for the purpose (low number of filled bunches, null crossing angle and a β^* equal to 19.2 m instead of 0.25-0.8 m). The bunch luminosity is given by

$$L_b = \frac{f_r \, n_1 \, n_2}{2\pi \, \Sigma_x \, \Sigma_y}$$

Σ_x (and in an analogous way Σ_y) can be determined using the instantaneous luminosity $R(\Delta x)$ measured as a function of the distance Δx between the two beams along the trasversal direction x.

$$\Sigma_x = \frac{1}{\sqrt{2\pi}} \frac{\int R(\Delta x) d\Delta x}{R(0)} \tag{1.65}$$

If $R(\Delta x)$ is Gaussian, Σ_x will be the RMS of the distribution. Since $R(\Delta x)$ is normalized, it is possible to use every quantity that is proportional to luminosity to determine the calibration curve. Combining 1.39 and 1.65, it is possible to calculate the visible cross

section as

$$\sigma_{vis} = \mu_{vis}^{MAX} \frac{2\pi \, \Sigma_x \, \Sigma_y}{n_1 \, n_2} \tag{1.66}$$

where μ_{vis}^{MAX} is the maximum number of visible interaction per bunch crossing calculated in the peak of the scan curve.

Chapter 2

LUCID-2

2.1 Introduction

In this chapter will be analyzed LUCID-2, the ATLAS main luminometer during Run-2. To understand the basic working principle of LUCID is necessary a brief introduction to LHC and the ATLAS detector.

2.2 LHC

LHC (Large Hadron Collider) is an accelerator of CERN in Geneve. It was built to overcome the potential for discovery of LEP (the previous CERN accelerator) and of Tevatron (Fermilab accelerator) and to investigate events with an energy threshold greater than TeV. It consists in a ring whose length is 27 km made up of superconductive magnets which allow to curve the beams inside. However, LHC is only the last stage of an accelerator chain (fig 2.1)[10] constituted by the previous accelerators that were used at CERN. It is made by:

- LINAC2: is a linear accelerator that takes protons from the source and accelerate them up to 50 MeV
- Proton Synchrotron Boost (PSB): accelerate protons coming from LINAC2 up to 1.4 GeV
- Proton Synchrotron (PS): accelerate particles up to 28 GeV and separates bunches of 25 ns
- Super Proton Synchrotron (SPS): is the last stage before LHC and raises the energy up to 450 GeV

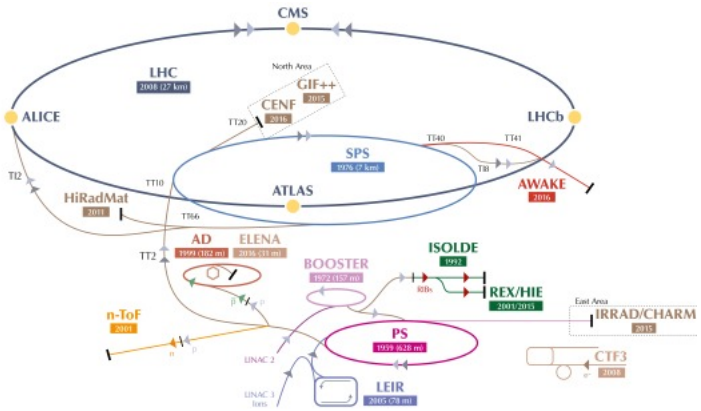

Figure 2.1: Scheme of LHC where the old CERN accelerators are also present, now used as pre-accelerators for the LHC beams before injection

Two beams circulate within the LHC, which can be either proton or ion, in opposite directions which are then made to collide at certain points, called interaction points (IP). The beams, as mentioned above, are divided into 3564 packets (bunch) as the acceleration system was not designed to accelerate continuous beams. However, of the 3564 available bunches, only 2544 can be filled. In physics runs there is a bunch crossing every 25 ns. The maximum design center-of-mass energy is 14 TeV, but in Run-2 a center-of-mass energy of 13 TeV was reached. The parameters of the beams are shown in the table (2.1). The 4 experiments present at LHC were placed in correspondence

Parameter	2018	Design value
Beam energy [TeV]	6.5	7
β^* at IP 1[m]	0.25	0.55
Bunch spacing [ns]	25	25
Maximum number of bunch	2544	2808
Mean bunch intensity [protons/bunch]	1.15×10^{11}	1.5×10^{11}
Peak luminosity [$cm^{-2}s^{-1}$]	2.0×10^{34}	1×10^{34}
Maximum number of events per BCID	60	19

Table 2.1: Current LHC performance compared to design values

with the IPs: ATLAS, CMS, ALICE and LHCb.

- ATLAS (A Toroidal LHC ApparatuS) aims to study the Higgs boson, make precision measurements of the standard model and look for any signs of physics beyond the standard model

- CMS (Compact Muon Solenoid) uses different and complementary detector technologies
- ALICE (A Large Ion Collider Experiment) studies the behavior of quarks under conditions of high temperature and high energy density, it is the only experiment present at LHC aimed at the study of collisions between heavy ions
- LHCb (LHC beauty) instead deals with the physics of flavor and the violation of symmetries such as CP violation.

The in-depth analysis of each experiment is beyond the scope of the thesis so only the ATLAS experiment will be illustrated in detail.

2.3 ATLAS

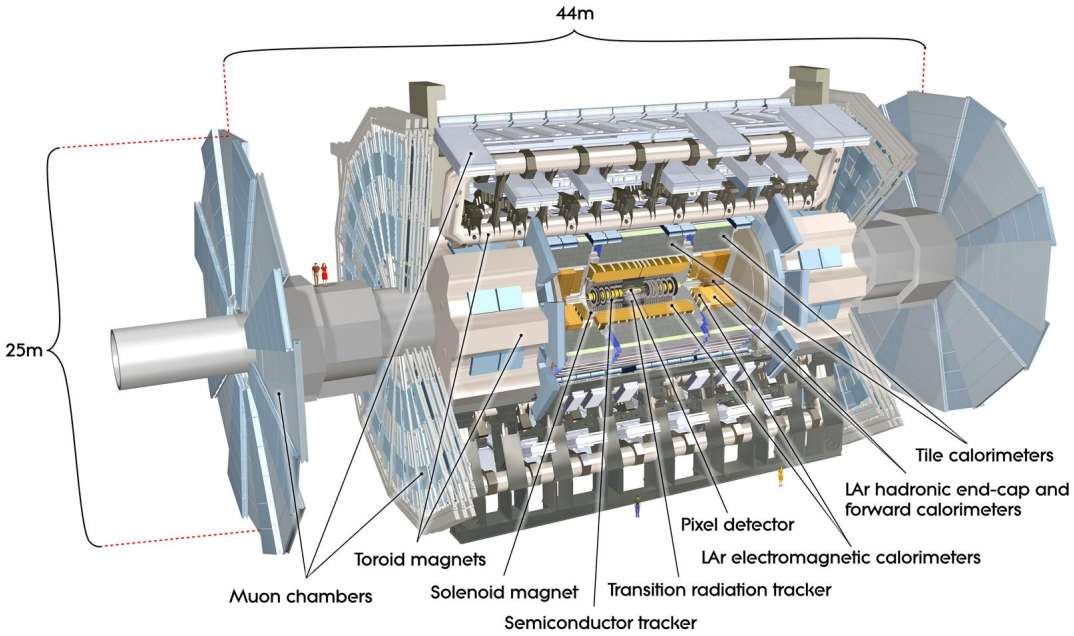

Figure 2.2: The ATLAS experiment

The ATLAS (Fig. 2.2) [11] detector is one of the general purpose experiments at LHC and it is nominally forward-backward symmetric with respect to the interaction point. Its dimension are 25 m in height and 44 m in length, while the weight is approximately 7000 tones. It can be divided into 4 different parts: inner detector, calorimeter, muon chamber and magnets.

- Inner detector: inner detector (ID) is the closest part to the interaction point and has the purpose of measuring the momentum of the charged particles passing through it reconstructing its trajectory. It consists of 3 types of trackers immersed in a strong solenoidal magnetic field of intensity equal to 2 T. From the innermost to the outermost they are: Pixel Detector, Semiconductor Tracker and Transition Radiation Tracker. It is made of light materials to avoid that the trajectory of the particle traversing it is too much influenced by multiple scattering. It's able to detect only charged particles.

- Calorimeters: the purpose of calorimeters is to measure the energy of all particles, except the muons, which pass through it. ATLAS, having to measure energy of photons, electrons and hadrons, it is equipped with two different types of calorimeters: the electromagnetic one and the hadronic one. The electromagnetic calorimeter, called Liquid Argon (LAr), exploits liquid argon to induce bremsstrahlung and creation of electron-positron pair to measure the energy of photons and electrons. The hadronic calorimeter (TileCal) instead uses iron as an absorber and scintillating plates as active material

- Muon chamber: the purpose of the muon spectrometer is to measure the energy of muons. To do this, it uses a principle similar to that of trackers: it measures the trajectory of muons which, being immersed in a magnetic field, is curved and from the radius of curvature it is possible to trace their energy. Is the most external part of the ATLAS detector since muons are particles that do not interact a lot with matter and therefore a large volume is needed to be able to them reveal.

- Magnets: ATLAS has 2 different types of magnets: solenoidal magnets and toroidal magnets. The first one produces a solenoidal magnetic field of 2 T inside the tracker, while the last one produces a toroidal magnetic filed inside the muon chamber.

By combining the information obtained from the fore-mentioned detectors it is possible to understand which particles were produced in the collisions and measure dynamic quantities such as their energy or momentum. Another important part of the detector consists of luminometers. In this thesis it will be treated in depth only LUCID as a complete discussion of all luminometers is not relevant this thesis.

2.4 LUCID-2

2.4.1 Introduction

A new luminosity detector for the ATLAS experiment has been designed in 2013, installed in 2014 and commissioned in 2015. The detector is called LUCID-2 and consists

of several small Cherenkov detectors for luminosity measurements and luminosity monitoring. The novelty of the LUCID-2 detector is that it uses the thin quartz windows of photomultipliers as Cherenkov medium and that it uses small amounts of radioactive ^{207}Bi sources deposited on to these windows to monitor the gain stability of the photomultipliers. The result is a fast and accurate luminosity determination that can be kept stable during many months of data taking.

The aim of the new LUCID-2 detector is to measure luminosity by not only counting hits (signals over threshold) in the detector but also by integrating the signals with Flash ADCs (FADCs). The advantage with the latter so-called charge integration method is that it can in principle work at the very high number of pp-interactions per bunch crossing expected in LHC Runs 2 and 3.

Some 2808 different colliding bunch pairs can be filled in the LHC and it is in many cases very useful or even essential to measure luminosity for each individual pair of colliding bunches making it another goal of LUCID. Moreover, LUCID-2 is the only detector in ATLAS that can measure luminosity for the individual bunches by charge integration.

In addition, LUCID-2 provides LHC with fast luminosity and beam background information (every 1-2 seconds). Fast luminosity feedback on such time scales is an essential element for beam optimization.

2.4.2 Structure

LUCID (LUminosity mesurement using a Cherenkov Integrating Detector) is divided into 2 modules (Fig 2.3) (one in side A and one in side C) placed 17 m away from the interaction point in a symmetric way. Each module is made of 16 photomultiplier tubes(PMT) grouped in 4 blocks with 4 PMTs and of 4 optic fibers coupled with a PMT for the readout. PMTs are attached to the beampipe through a carbon fiber support. Attached to the support there are also a sensor to monitor the temperature and the cooling system. The measurement system based on the fiber is made of 4 fibers of 2 m length coupled with a PMT. Fibers have a double role: they are used both as a Cherenkov radiator both as a transmission medium to bring Cherenkov light to the PMT since the PMT are placed in a less radioactive area.

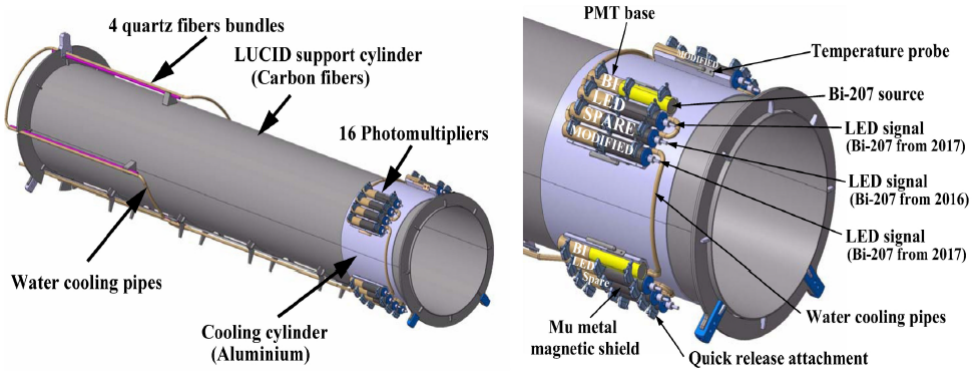

Figure 2.3: The left drawing shows the LUCID support cylinder with the four quartz bundles at the back and the 16 photomultipliers at the front. The right drawing shows the support and cooling structure of the photomultipliers.

Each PMT is made of a quartz window that is used as a Cherenkov radiator. Behind it there is a photoelectric material whose purpose is to convert Cherenkov photons into photoelectrons. This electron signal is multiplied by a chain of dinodes with a gain of up to 10^6. The signal is then read by an electronic board called LUCROD.

In LUCID-2 there are 4 different types of PMTs:

- Bi: 4 Hamamatsu R760 PMTs with a diameter of 10mm on whose quartz window is deposited of ^{207}Bi for calibration
- Bi2: 4 Hamamatsu R760 PMTs with a diameter of 10mm on whose quartz window is deposited of ^{207}Bi for calibration. The difference with Bi is that the Bi were the first one to use the ^{207}Bi for calibration
- BiM: 4 Hamamatsu R760 PMTs with a diameter of 7mm. The acceptance has been reduce by placing an aluminum foil on the window. On quartz window is deposited of ^{207}Bi for calibration
- Spare: 4 Hamamatsu R760 PMTs with a diameter of 10mm on whose quartz window is deposited of ^{207}Bi for calibration. They are used as substitute in case of malfunction of the other PMTs

2.4.3 Calibration

It was observed that PMTs age due to the charge they register and due to the radiation of the environment. One of the effects of the aging is the reduction of the PMT gain. To monitor and adjust the gain reduction two different techniques(fig 2.4) were used. The first one consist in placing a radioactive material(in this case ^{207}Bi) on the PMT window.

This technique is used to calibrate Bi, Bi2, BiM and SPARE. The second one involves LEDs and is used to calibrate the fibers. The idea behind them is the same: compare, after every physics run, the signal of the ^{207}Bi or of the LED (that are supposed to not vary) with a reference signal to estimate the gain loss. In case of variations in the gain the high voltage (HV) of the PMT is adjusted in order to restore the gain. After that, there is a calibration run to check if the calibration was successful. If not, there is another calibration and a verification run. The fiber PMT calibration using LED light was never accurate. Because of this a new hybrid system that uses both LEDs and bismuth was designed and will be used in Run 3, see Chapter 3.

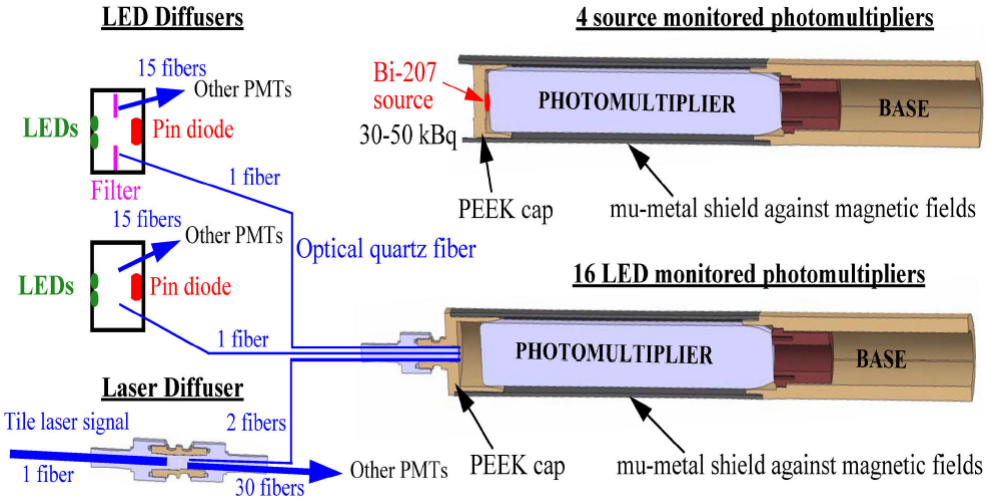

Figure 2.4: Schematic view of the LUCID-2 relative calibration system for one detector module

Calibration via bismuth

The reason why ^{207}Bi is a useful source for relative calibration is that in 11.5% of all disintegrations it emits internal conversions electrons with an energy of 482, 554, 566, 976, 1048 or 1060 KeV and these energies are all above the Cherenkov threshold in quartz. However only electrons with an energy above 900 KeV are expected to penetrate fully the quartz window without being stopped. The half-life of ^{207}Bi is 33 years which means that the source will not change rate significantly during the detector lifetime. To monitor the stability of the gain are measured both the average charge and the average amplitude of the signals for each PMT. From these measures it is possible to estimate the gain and, in case of deviations from the reference value, we modify the HV to return the gain to the desired value.

The main reason for using a calibration system based on radioactive sources deposited on the quartz window of the PMTs is that it is intrinsically free from possible instabilities

of the input light and from possible degradation of the optical fibers transporting this light due to radiation damage. The wavelength of Cherenkov light is also different from that of LED light which can be important since the efficiency of the photocathodes is wavelength dependent.

A critical parameter to be considered with this method is the activity of the deposited source. This has to be large enough to allow for calibration runs to provide sufficient statistics in a reasonable time, but not too large in order not to interfere with the luminosity measurement during data-taking. The background produced by the Bismuth is in fact present all the time. While this is not an issue during normal high luminosity operation, problems can arise when performing data takings in special conditions, such as the Van der Meer scans at very low luminosity needed for the absolute luminosity calibration. Indeed, this was one of the main reasons at the beginning for not equipping all PMTs with radioactive sources but keeping LED/LASER-calibrated PMTs as well. A typical activity between 30 and 45 kBq for the various PMTs has been used. This activity proved to perfectly meet the two limitations/requirements on efficiency and background.

Due to the good result obtained with this technique, from 2017 all the PMTs used this technique for calibration and only the fibers were calibrated via LED/LASER signals.

Calibration via LEDs

In this case, it's used the monochromatic light produced by the LED. This light is divided and sent to the PMTs. Analyzing the output signals of the PMTs it is possible to measure the gain and, if it's necessary, modify the high voltage.

This method has 2 main problems:

- LED light can fluctuate. To monitor these fluctuations the LED light is sent to a sensor (PIN-diode) placed in an area far away from the collision in order to avoid radiation damage of the PMT
- LED has a different spectrum with respect to Cherenkov radiation. Thus, a different quantum efficiency between different wavelength can induce a different response of the PMT between particles and LED light

2.4.4 Electronics

LUCID-2 electronic was projected to count the number of hits and to integrate charge using Flash-ADCs (FADCs). The advantage of a measurement of integrated pulses is that it is proportional to the number of particles going through the detector and it is therefore not affected by the already mentioned migration problem. Charge measurements can also be applied to fiber bundles not suitable for hit counting. On the other hand, charge integration algorithms are more sensitive to PMT gain variations, making the calibration procedure crucial.

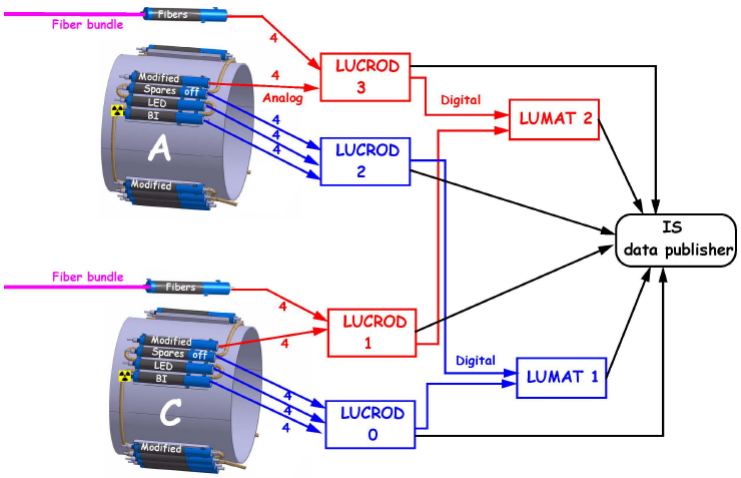

Figure 2.5: Block diagram of the electronics for the LUCID-2 detector.

In fig 2.5 the block diagram of the electronics used for the LUCID-2 detectors is shown. The photomultiplier pulses are fed to 4 LUCROD boards where signals are amplified, digitalized, discriminated and integrated. Hit patterns corresponding to all possible bunch crossings are transmitted to two custom VME boards (LUMAT boards) located about 100 m away, via optical links. As in LUCID-1, the LUMAT boards use hits to produce the counts needed by luminosity algorithms that uses signals from the two sides of the detector.

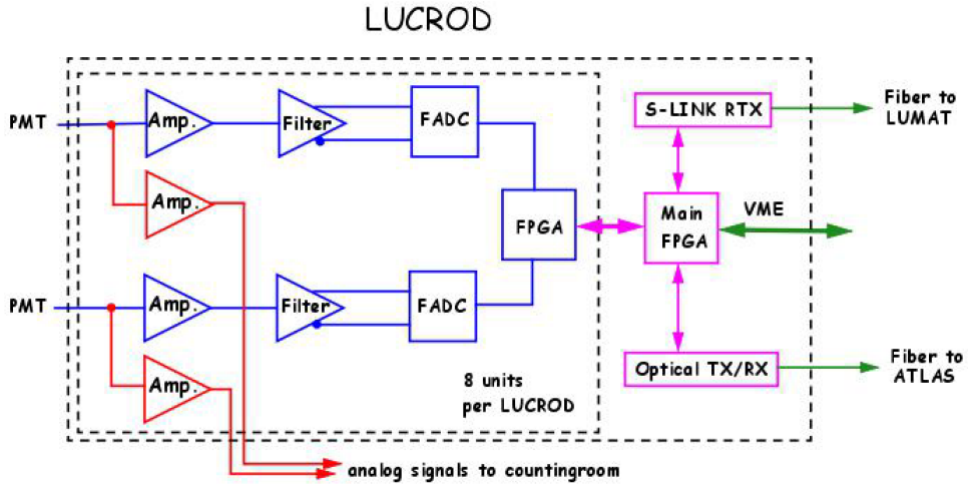

Figure 2.6: Block diagram of the LUCROD board.

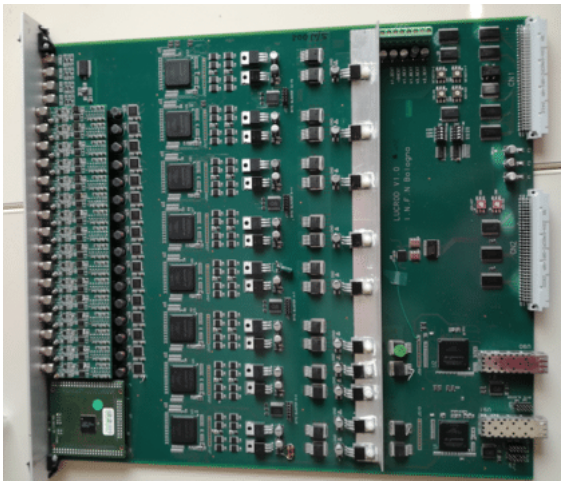

Figure 2.7: Picture of the LUCROD board.

In fig 2.6 the scheme for the LUCROD board is reported. The LUCROD board is a custom 9U VME board designed by the Electronics Lab of the Bologna Section of INFN. The board features 16 lemo analog inputs, 16 lemo analog outputs (amplified copies of the inputs), four lemo digital I/O channels for triggering and debugging purposes, as well as JTAG and optical-link connectors. In additions, it holds a TTCrq5 to receive external synchronization signals, and optical transceivers to deliver digital information.

Each LUCROD input is fitted with two independent and programmable amplifiers (with a gain of up to a factor of 16), one serving the analog output and the other one feeding a 320/480MHz FADC with 12-bit resolution (Equivalent Number of Bit ' 10) and 1.5V dynamic range. The zero level of the signals is adjustable with dedicated DACs.

Each LUCROD board hosts one group of eight channel FPGAs and another group of two main FPGAs. The former are directly connected to the inputs, each receiving the digitized data of two channels. The latter provides the VME interfaces and the interface to the optical transceivers. All data buses are 16-bit, while the VME interface have both 16 and 32 bits.

Since the LUCROD boards are located close to the PMTs, in an area that cannot be accessed during LHC running periods, a dedicated firmware was developed to allow for loading and changing the firmware itself, both via VME and via another VME board acting as a VME blaster.

2.4.5 Algorithms

There are 2 types of algorithms: online and offline algorithms. The first ones are used to monitor in real time the performance of the machine. For this reason they must be fast algorithms since they must measure luminosity every second. The luminosity measured by the second one has to be measured with higher precision since it will be used for

cross section (σ) measurements. Since there isn't a time limit, these algorithms are more complex and can take into account some effects that were neglected in online algorithms like the background subtraction.

Online algorithms

The online algorithms for calculating luminosity serve to provide in real time information on accelerator performance. The calculation and publication of the instantaneous luminosity are carried out by Online Luminosity Calculator (OLC) and are shown in the ATLAS control room. They are also sent to the LHC at a frequency of about 1 Hz to set the machine parameters correctly. The purpose of OLC is to collect information on the number of events/hits, on the number of colliding bunches to be able to measure the average number of colliding events per bunch (μ). Due to the tightness of time, some effects will be neglected , for example the background subtraction.

In LUCID 5 algorithms are implemented:

- Hit_OR: returns the average number of hits per bunch crossing (BC). In this algorithm, there is a hit if there is at least one signal in one of the 16 PMTs in at least one of the two sides in the same BCID
- Hit_AND: returns the average number of hits per BC. In this case we have an hit if there is at least one signal in one of the 16 PMTs in both sides in the same BCID
- Event_OR: returns the number of events in which there is at least one hit in a PMT in at least one side
- Event_AND: returns the number of events in which there is at least one hit in a PMT in both sides
- Charge: returns the value of the charge released in the PMTs. The charge released, being proportional to the number of particles passing through the quartz window of the PMT, is proportional to the luminosity.

The advantage of using event or hit algorithms is that they are less sensitive to gain fluctuations of the PMTs with respect to charge algorithms, so they have a better temporal stability. On the other hand, these algorithms are strongly dependent on the assumption that the number of hits follows the statistic of Poisson, assumption that can be false due to the background, both physical and instrumental. Moreover, for high values of μ we fall into the phenomenon of saturation, i. e. when we have an hit for every bunch crossing. In this case, eqs 1.58, 1.59 and 1.63 diverge and is not possible to measure μ. Charge algorithms instead are linear with respect to μ and, in principle, is applicable to every value of μ, but is very sensitive to gain fluctuations.

Offline algorithms

LUCID-2 implements all the online algorithms also offline. Moreover, also OR-algorithms are implemented for each side (ORA and ORB). Since there is no limit time for this kind of algorithms, we can take into account effects that before were neglected like the background subtraction.

During offline analysis, there are other detectors that can contribute to a complementary measurement of luminosity. These are the inner detector and the calorimeters. The final luminosity measurement is very precise thanks to the combination of all these detectors and algorithms.

Chapter 3

LUCID-3

3.1 Introduction

LUCID-2 won't be able to face the challenges during High Luminosity LHC (HL-LHC) so a new detector (LUCID-3) must be built. After analyzing all the reasons why LUCID-2 won't be compatible with the ATLAS physics program for HL-LHC, the possible designs for LUCID-3 will be analyzed and, at the end, there will be a description of the prototypes of LUCID-3 that will be tested during Run-3.

3.2 Physics Motivations

	Baseline	Ultimate
Number of colliding bunches in ATLAS	2748	2748
Peak luminosity [$cm^{-2}s^{-1}$]	5×10^{34}	7.5×10^{34}
Peak pile-up [collisions/event]	131	197
Luminosity leveling time [hours]	7.4	3.6
End-of-fill luminosity [$cm^{-2}s^{-1}$]	3×10^{34}	4.5×10^{34}
Peak pile-up line-density [events/mm]	1.3	1.95
Average pile-up line-density [events/mm]	0.8	1.2
RMS time spread of the luminous region [ps]	178	178
Integrated luminosity [fb^{-1}/year]	262	326

Table 3.1: Two scenarios for the beam conditions expected for Run 4 and beyond

The expected LHC conditions in Run-4 are summarized in Table 3.1 and include a "baseline" and "ultimate" scenario, with a peak luminosity of $5 \times 10^{34} cm^{-2} s^{-1}$ (peak μ of about 130) and $7.5 \times 10^{34} cm^{-2} s^{-1}$ (peak μ of about 200) respectively. In both cases LHC

will run the luminosity-leveling mode in order to ensure a safe operation of the detectors and ensure an efficient use of the beam allowing a reach of $3000 fb^{-1}$ and $4000 fb^{-1}$ respectively. The ultimate scenario will probably be reached after Run-4 although the experiments require and as fast as possible ramp-up of LHC to this condition. Therefore, all the detectors must be designed in order to cope with these ultimate conditions.

3.2.1 Requirements for offline luminosity

Precision measurements foreseen by the ATLAS physics program[13][14][15] in Run-4, including in the Higgs sector, call for a precision of 1% in the offline measurement of the integrated luminosity, to be compared to the 1.7% achieved in Run-2 on the full data sample. This limits to the sub-percent level the various contribution to the uncertainty, the main ones being Van der Meer absolute calibration, the calibration transfer for the low- to the high-luminosity regimes and the long term stability.

The stringent requirement on precision calls for a multiplicity of luminosity detectors including at least 2, preferably 3, detectors VdM-calibratable and being able to measure at high-luminosity. LUCID-3 is expected to be one of these detectors. Additional detectors with a high level level of linearity must be cross-calibrated in the VdM luminosity regime and will be used for long-term systematic assessment and/or for non-linearity correction of the main luminometers and must be cross-calibrated at least at high-luminosity.

The same strategy was applied in Run-2, although the needed redundancy could not be achieved since LUCID was the only detector able to provide a per-bunch measurement in all the luminosity regimes. The limitations of the LUCD measurement in Run-2 and their implication for Run-4 will be discussed later (see section 3.2.3).

3.2.2 Requirements for online luminosity

Online luminosity measurement does not have such stringent requirements as the offline in terms of absolute precision but additional features must be ensured to ensure a proper beam operation by LHC, in particular for the luminosity leveling operation and for an efficient use of the beam by ATLAS. The main requirements of the online luminosity measurement are[16]:

- capability to measure luminosity on a bunch-by-bunch basis with a precision of $2-3\%$;
- provide the delivered luminosity without dead-time and independently of the ATLAS TDAQ at a rate of about 1Hz;
- operate safely in all beam modes, in particular outside STABLE BEAMS;

- redundancy and flexibility to immediately switch among different measurements in case of detector malfunctioning to avoid glitches in the luminosity provided to LHC;

- linearity and long-term stability, s for the offline measurement.

All these features are available now and will be ensured by LUCID also in Run-4, although concerns about the ability to measure in time-intervals as short as one second must be solved while avoiding algorithm saturation.

3.2.3 Limitations of LUCID-2 at HL-LHC

One of the main concerns about using Event-counting and Hit-counting algorithms to measure luminosity is the saturation effect, namely the fact that the detector observes an event (or a hit) in each bunch crossing during a luminosity block. In this case, the logarithmic formula used to linearize the measurement fails and there is no way to determine the luminosity.

Already in Run-2, event-counting algorithms saturated at $\mu \approx 20 - 30$ (depending on the type of algorithm), while hit-counting algorithms did not saturate in the probed μ-range, and are not expected to saturate until $\mu \approx 110 - 120$. This μ-value is too low for for Run-4 operation. One possibility to avoid saturation is to lower the geometrical acceptance of the detector, either by reducing the active area of the sensors or by moving them into a region with lower particle fluxes. The first option was tested during Run-2 by installing MOD-PMTs.

MOD-PMTs were produced by Hamamatsu starting from the standard R760, upon request of the LUCID group, in order to reduce the detector acceptance to about a half. These photomultipliers have a ring of aluminum deposited on the inside of their windows. This ring reduces the acceptance of the photomultipliers. However, Monte Carlo simulations predicted that the smaller acceptance was obtained at the cost of a larger μ-dependence, as it was indeed observed in data. There are also indications that the function needed to correct for μ-dependence might be more complex than the simple quadratic formula applied to the standard PMTs in the μ-range probed in Run-2. Even if it is not possible to predict the non-linearity at the higher μ-values of Run-4, the larger effect of the MOD-PMTs suggests that a detector based on MOD-PMTs might run into problems in the Run-4 scenario.

The saturation effect does not affect the charge-integrating algorithms, where the observed charge is proportional to the luminosity, provided that the dynamic range of the electronic chain and the working conditions are correctly dimensioned. This was the case for Run-2 by working with a PMT gain of the order of 10^5 which allowed to have sensitivity in both the low- and high-luminosity range.

3.3 Introduction of the main strategy

The present LUCID-2 detector is, as discussed previously, using two main methods for measuring luminosity with more than 100 different algorithms. One of these methods is counting hits, i.e. pulses above a certain threshold, and another one is counting charge, i.e. the integral of pulses.

One of the main problems with Hit-counting is the so called μ-correction. This is a correction that has to be applied to the logarithmic formula that is used to calculate luminosity from the number of hits. This correction increases with μ and, since the average μ is expected to increase by a factor of 2.5-3.8, the correction will be larger during Run-4. Another, and even more serious problem, is the Hit-saturation, which means that there are hits in every bunch crossing during a lumi-block. If this happens, LUCID is no more able to measure luminosity using this algorithm. A way around is to use MOD-PMTs (Fig 3.1).

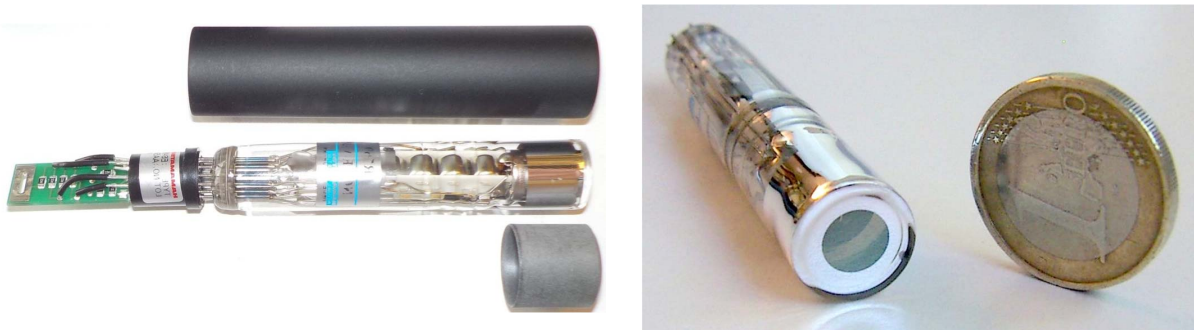

Figure 3.1: The photo on the left shows a Hamamatsu R760 photomultiplier with its base and mu-metal magnetic shield as well as the peek cap that is glued over the front of the PMT to seal in the ^{207}Bi source. The photo on the right shows a special modified PMT that has a white ring of aluminium deposited on the inside of the PMT window.

The drawback with CHARGE-counting is that it is more sensitive to photomultiplier gain variations. The charge is basically proportional to the gain while one percent reduction of the PMT gain typically gives only a $0.3 - 0.4\%$ reduction of the Hit-luminosity. A method has therefore been developed where Hit-counting (without a μ-correction) is used to stabilize the Charge-counting measurement.

The most obvious design of a new LUCID-3[17] detector would be a copy of the present LUCID-2 detector. In this case the detector would again be attached to the VJ beampipe and sit inside a new beampipe support cone. A serious complication will be the new vacuum equipment (the VAX) that will be installed close to the present LUCID-2 location in LHC Run-4 (Fig 3.2).

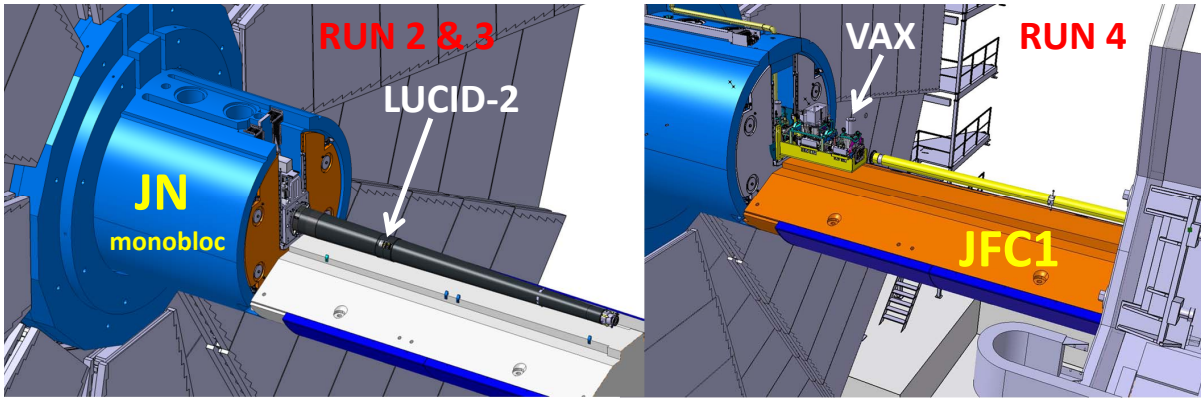

Figure 3.2: The drawing on the left shows the location of the present LUCID-2 detector in the beampipe support cone. In this drawing only the bottom part of the forward shielding (JFC1) is installed. The picture on the right shows the new vacuum equipment (VAX) that will be installed in run 4.

Another possibility would be to attach the new detector to one of the forward shielding pieces. The piece that is under consideration is JFC3 (see Fig. 3.3). This shielding piece is, like all forward shielding pieces, removed during each end-of-year-shutdown (EOYS). The new detector would thus be available for maintenance in the buffer zone of SX1 surface building every winter. The yearly maintenance will consist mostly of changing photomultipliers and this would be more difficult if the detector is located inside the VJ cone.

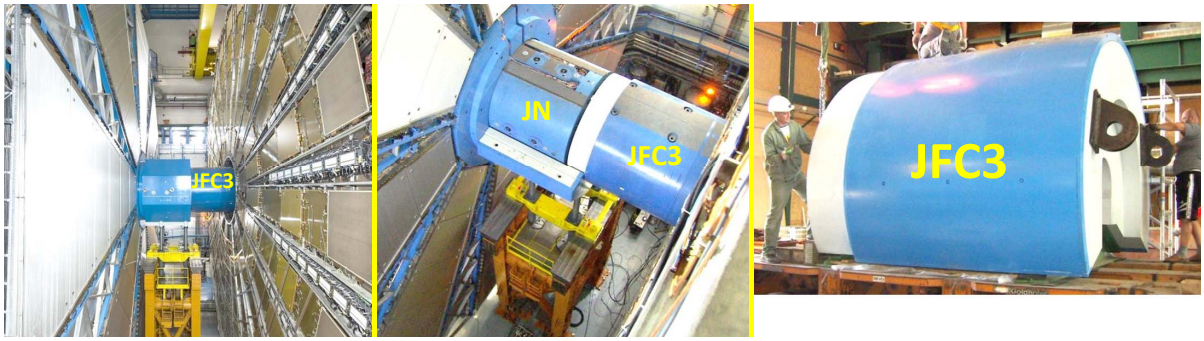

Figure 3.3: Photos of the forward shielding piece JFC3 during different stages of an ATLAS opening. The left photo shows the situation when all shielding is installed. The top octagonal shielding piece has been removed in the middle photo. The JFC3 shielding piece after removal from ATLAS is shown in the photo on the right.

The main advantages of a detector attached to the shielding instead of to the beampipe would be:

- The detector and services will be more accessible in SX1 during shutdowns;
- No interference with the VAX or the beampipe design;
- Less radiation and saturation problem at a larger distance to beampipe
- No need for water cooling during beampipe bakeout (if JFC3 is not installed).

The main disadvantages would be:

- The detector has to be disconnected and connected every shutdown;
- The location of JFC3 and LUCID might change slightly every year;
- Some additional machining to the shielding might be needed.

In addition to having two main methods to measure luminosity and two possible locations to install the detector, there are also two possible detector technologies. The main detector in the LHC Run-2 was a detector based on Cherenkov light produced in the quartz window of the PMTs. However, also 4 bundles of 37 quartz fibers coupled with PMTs have been installed on each side. Any deterioration of the light transmission of the fibers in latter detector cannot be monitored and the PMT gain can only be monitored by LED signals. Only the Charge measurement method can be used with this detector. The FIBER detector has for the above reasons not been able to produce a stable luminosity measurement during LHC Run-2. With improved methods of gain monitoring it could, however, be a contender for LHC Run-4 where the increase in luminosity results in a potential increase of radiation damage to a PMT detector.

There are three different LUCID-3 detectors under consideration:

- A PMT detector attached to the shielding;
- A FIBER detector attached to the VAX and beampipe support cone;
- A FIBER detector attached to the shielding

Taking into account the above discussed advantages and disadvantages of different methods, locations and detector technologies it has been decided that the baseline LUCID-3 detector will be a PMT detector attached to the JFC3 shielding. A FIBER detector located around the beampipe is regarded as the main back-up possibility but also a FIBER detector attached to the JFC3 shielding is being considered. The final choice of detector will be determined based on the performance of prototype detectors that are installed already before LHC Run-3.

3.4 A LUCID-3 detector attached to the shielding

Fig 3.4 shows what a Fiber + PMT detector that is attached to the shielding would look like. Eight photomultipliers would side on the sides of the beampipe hole in each one of the two JFC3 shielding pieces. The PMTs would be attached with a rail system so that the PMTs can be quickly pulled out of the beampipe hole during maintenance work. One could in addition envision having several bundles of quartz fibers running together at the top of the beampipe hole in the shielding.

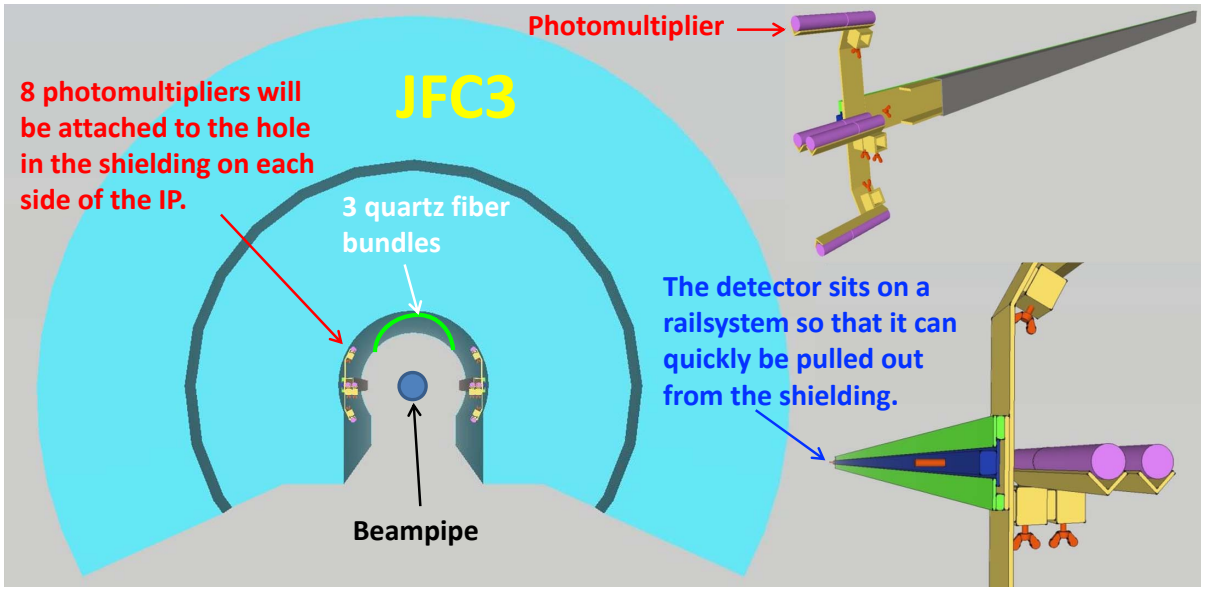

Figure 3.4: A front-view of the JFC3 forward shielding piece with the location of the PMT detector.

A side view of the detector is shown in Fig 3.5. The services of the photomultipliers would be running along the beampipe hole to the back where they would go up to the top of JFC3 shielding piece where connectors would be located. The fiber bundles would also go to the back of the shielding and then up to the top of the shielding where photomultipliers would be located.

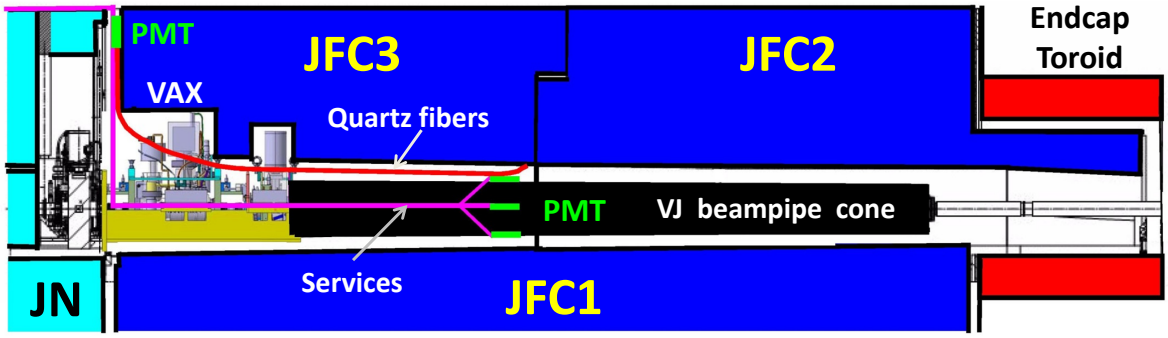

Figure 3.5: A side-view of a future LUCID-3 detector that is attached to the JFC3 forward shielding piece.

An important factor which makes it possible to use the JFC3 shielding piece as a LUCID support without too many modifications is the 80 mm gap between the JFC3 and the JN shielding. This gap is shown in the images in fig 3.6. The idea is that this gap would allow services from a PMT detector to go to the top of the JFC3 shielding where they could be connected to the existing LUCID-2 services. A FIBER detector would have, in addition, photomultipliers and an LED calibration system installed in this gap.

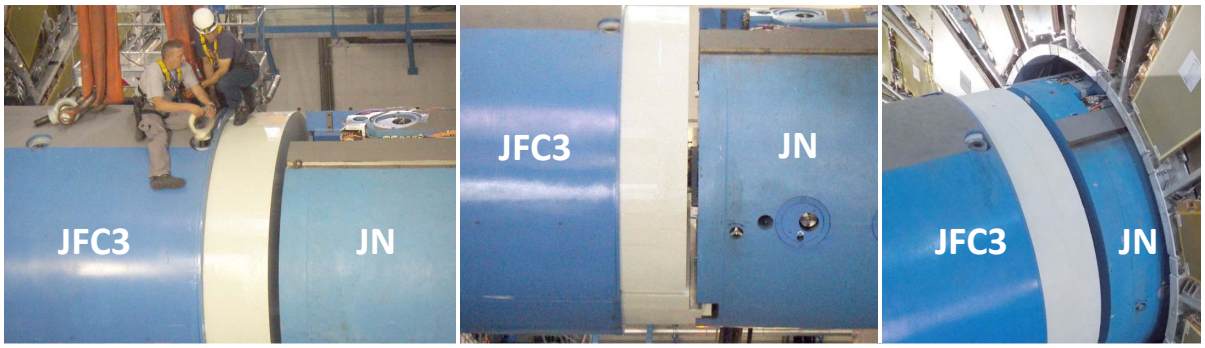

Figure 3.6: Three photos that show the gap between the JFC3 forward shielding piece and the permanently installed JN shielding. Services from the PMT detector would go up from the beampipe region to the top in this gap. A fiber detector attached to JFC3 would also have photomultipliers and LED systems in this gap.

Since the JFC3 shielding has to be disconnected in every EOYS, it is important that the number of connectors, and therefore the number of channels, are kept to a minimum. The aim is that the people responsible for lifting out and in the JFC3 shielding will be able to disconnect and connect the detector without any expert intervention.

These services would have to go over the top of the JN-plus (see Fig 3.6). When

the top octagonal forward shielding piece is installed there is only a nominal 25 mm gap between this shielding piece and the JN-plug. It is envisioned to machine a 20 mm deep channel on top of the JN-plug to allow the LUCID services to pass over it.

3.4.1 A PMT detector on JFC3

The proposed PMT detector would sit on a rail system (Fig. 3.7) such that the detector could be slid forwards or backwards out of the shielding beampipe hole. The inside of the beampipe hole becomes very activated and so the idea is to quickly be able to get some distance between the people doing maintenance on the photomultipliers and the shielding hole. The rail-system will be attached in two places.

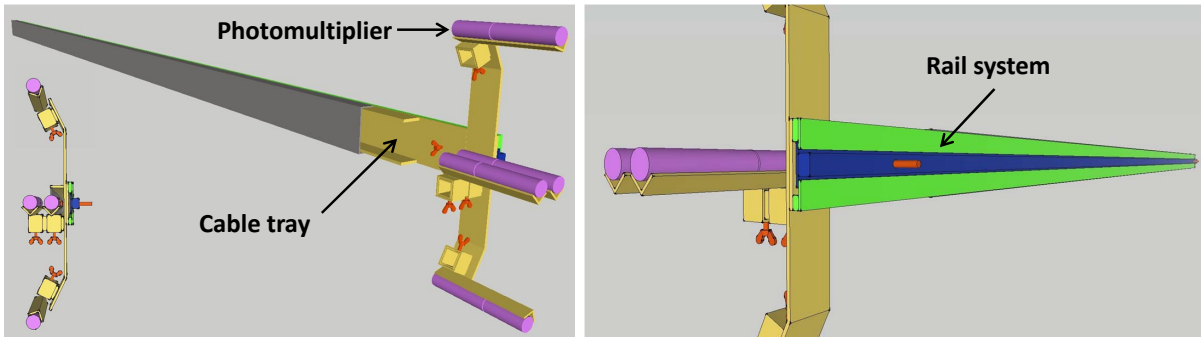

Figure 3.7: The PMT detector is attached to the forward shielding with a rail system so that it can easily be removed from the shielding during maintenance work in an end-of-year shutdown.

The services to the detector would run in a cable tray to the back of the shielding and then up to the top as discussed previously. At the back of the beampipe hole the services would have to make a 90 degree turn and that should not be a problem for the high-voltage (HV) cables but would be difficult for the CC50 signal cables that are thick and stiff. Special 90 degree BNC connectors would therefore be installed here. The cables going up to the top of the JFC3 shielding will be attached with clips to the shielding so that they can be removed quickly.

Another big advantage is that one can wait with installing JFC3 with the detector until a beampipe bake-out has been made.The proposed detector therefore does not need a cooling system together with the temperature probes that monitors LUCID temperatures during the bake-out (note that during normal operation LUCID-3, as well as the present LUCID-2, does not need any cooling and operates at room temperature). This is a considerable simplification over the present detector.

LUCID-2 has 16 PMTs on each side of the interaction point. The proposed new detector would have only 8. The reason for this is to minimize the number of connectors

that have to be disconnected before the JFC3 shielding can be removed. The position of the PMTs can change depending on the plane where the crossing angle is and on the results that will be obtained during Run-3.

The photomultipliers will be placed further away from the beamline in the new detector and it is expected that the particle density will be lower in the new locations. In the best case scenario, the standard PMTs can therefore be used also at the higher luminosity during LHC run 4. The simulations are not accurate enough to determine if this will indeed be the case and a measurement with a prototype detector is therefore proposed to take place during LHC run 3. If the rate turns out to be too high one would use MOD PMTs in a combination of standard PMTs.

3.4.2 A fiber detector on JFC3

Building a FIBER detector attached to the shielding will be more difficult than building a PMT detector. Radiation-hard optical fibers need to have both the core and the cladding made out of quartz. This means that the minimum bending radius is much larger than for standard optical fibers. In any case it is clear that no optical fibers can do a 90 degree turn at the end of the beampipe hole in the shielding. Fig. 3.8 shows a bottom-view drawing of the JFC3 shielding as it is proposed to look like in LHC run 4.

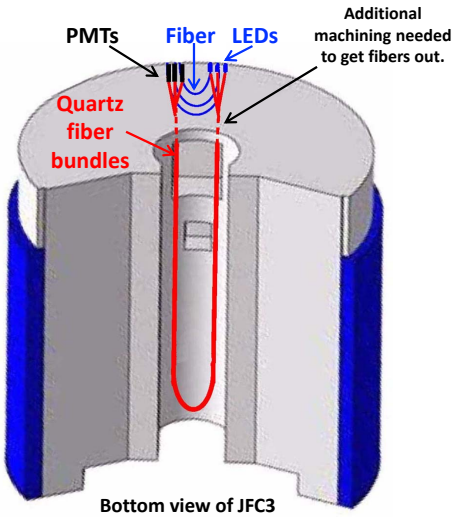

Figure 3.8: A bottom-view of the JFC3 forward shielding piece with the location of the fiber detector.

The detector could consist of three bundles of quartz fibers that are attached to the upper part of the beampipe hole. One end of the fibers would go to Hamamatsu R7459 photomultipliers with 28 mm diameter. These would be attached to the top of the shielding (see Fig. 3.5). The gain of these photomultipliers would be monitored with

radioactive ^{207}Bi sources applied to the edge of window. Any deterioration of the fibers due to radiation damage would be monitored by a set of LEDs connected to the other end of the fiber bundles and also attached at the top of the JFC3 shielding. The LEDs would also be connected directly to the PMTs so that the stability of the LEDs could be monitored.

3.5 A LUCID-3 detector attached to the beampipe

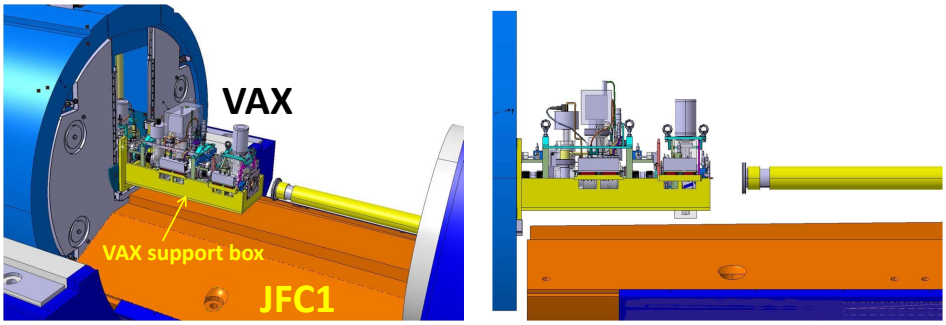

Figure 3.9: Drawing of the VAX equipment that will be installed in ATLAS prior to LHC run 4.

The new VAX equipment (Fig 3.9) will complicate the construction of a new LUCID detector around the beampipe. The present location of LUCID-2 at z = 17m is no longer available. The VAX equipment sits in the so-called support box which will not be removed during YETS. In case of problem with the equipment it will be lifted out remotely from the box because of the very large radiation levels in this region. This means that LUCID services and fibers can be attached to the outer sides of the support box but not pass over the VAX equipment.

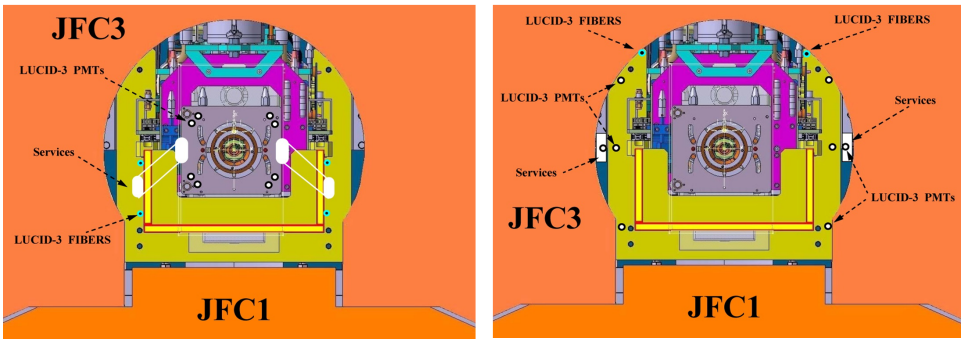

Figure 3.10: A front-view of the beampipe hole in the forward shielding and the new VAX equipment.The plot at the left shows the location of photomultipliers and fiber bundles if the detector is attached to the beampipe and the VAX. The plot at the right show instead the locations if the detector is attached to the JFC3 part of the forward shielding.

Fig. 3.10 shows a front-view of the beampipe hole in the JFC3 together with the VAX. One can see that there is sufficient clearance between the VAX support box and the JFC3 shielding to allow for services and fiber bundles. The locations of the photomultipliers in a PMT detector attached to the beampipe and to the JFC3 shielding are indicated in the figure.

If the detector is instead attached to the beampipe it would look like Fig. 3.11. The new beampipe support cone has not been designed yet and the cone indicated in this figure assumes it would have the same dimensions as the present one. A new PMT detector cannot be attached at the present location of Z = 17m but it looks like it can be installed about one meter closer to the IP. The services of the PMT detector will have to go back along the VAX support box. These services would have to include water and air pipes for cooling during the beampipe bake-out.

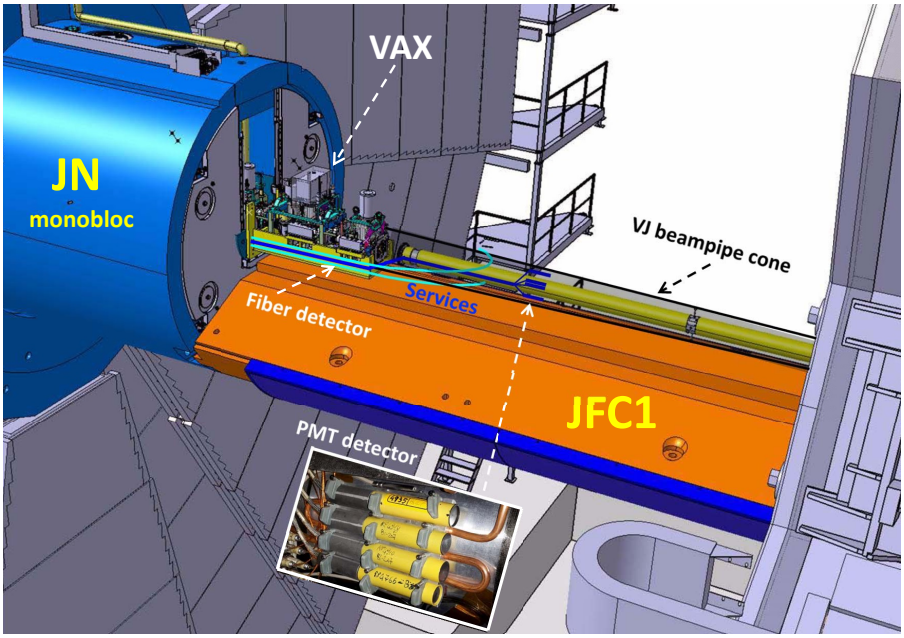

Figure 3.11: Drawing showing what a LUCID-3 detector attached to the VAX and the beampipe would look like. The beampipe cone has in this picture been assumed to have the same dimensions as the present one.

A new FIBER detector would follow one side of the VAX support box, go over or through the beampipe cone, and then back on the other side of the support box. Because of the large minimum bending radius that is needed for the fibers they cannot enter and leave the beampipe area on the same side of the support box. Fig. 3.5 shows a side-view of the detector.

3.5.1 A PMT detector attached to the beampipe

A new PMT detector around the beampipe could look very similar to the present LUCID-2 detector in Fig. 3.12. The photomultipliers would then sit on a water-cooled aluminum support attached to a carbon fiber cylinder. This cylinder would in turn be attached to the beampipe support cone.

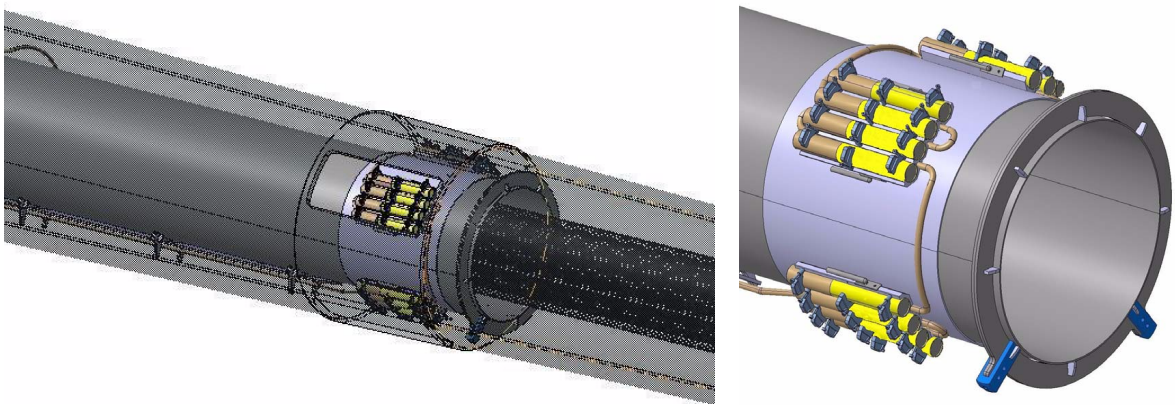

Figure 3.12: The drawings show the present LUCID-2 PMT detector. The drawing on the left shows the photomultipliers attached to a carbon fiber support cylinder that in turn is attached to the VJ beampipe support cone. The drawing to the right shows how the PMTs are attached to a water-cooled aluminium support system that is attached to the support cylinder.

The present LUCID-2 detector has 16 PMTs installed on each side of the IP and there is no reason that a new detector would have fewer channels. The main difference would be that modified Hamamatsu R760 PMTs or smaller PMTs would be needed in order to avoid Hit-saturation at the higher luminosity. A sub-set could be of standard type and be used to make VDM calibrations with a higher efficiency. The photomultipliers would be exposed to larger radiation levels than the present PMTs and one has to foresee that they have to be changed every year. Access to the photomultipliers during every YETS has therefore to be available. One has to make sure that the services and the connectors can survive the entire LHC run 4 since it would be impossible to change them.

3.5.2 A fiber detector around the beampipe

While it is quite obvious that a PMT detector attached to the forward shielding is preferred to a PMT detector attached to the beampipe, the best location of a FIBER detector is not so clear. The main problem with a FIBER detector on the shielding will be that additional machining of JFC3 will be perhaps be needed to get the fibers out of the beampipe hole and the photomultiplier might not fit in the 80 mm gap between the JF and JN. However, the radiation dose to fibers attached to the VAX is expected to be at least twice as large as to fibers attached to JFC3.

If the new beampipe support cone is made with a smaller diameter than the present one it is possible that fibers in the new detector could pass above and below the VJ cone as shown in Fig. 3.13. Two fiber bundles could go above and two below the VJ cone on each side of the IP. Each bundle would consist of 60-70 radiation hard quartz

fibers of type UVNSS 600/624/660. They would be placed in an aluminum or copper pipe to protect them from mechanical damage during shutdowns. Due to the extremely high radiation levels around the TAS collimator and the VAX equipment during EOYS it is not foreseen to be able to replace these fibers in case of radiation damage. It is therefore important that the fibers are tested with gamma and neutron sources so that their survival during LHC run 4 are ensured.

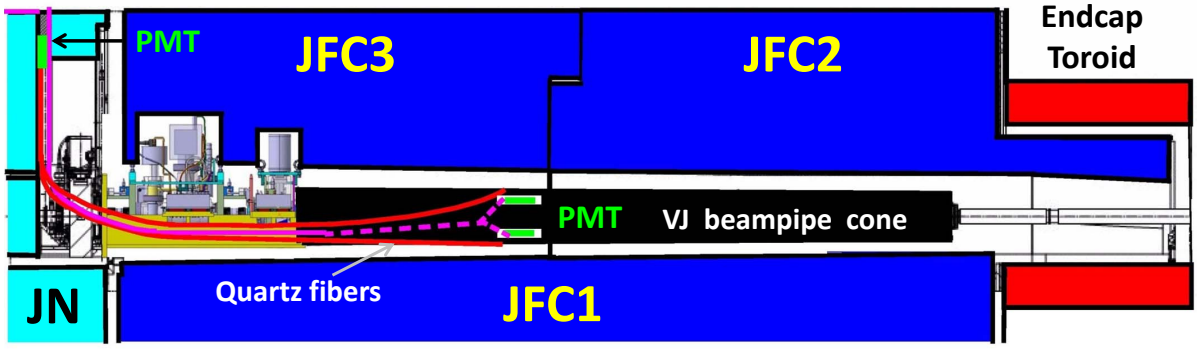

Figure 3.13: A side-view of a future LUCID-3 detector that is attached to the VAX and the beampipe.

The photomultipliers would be located in the same 65 mm gap between the JN plug and the JN monobloc where the present FIBER PMTs are located. The PMTs would be of the larger Hamamatsu R7459 type with 28 mm diameter. The larger size should make it possible to put radioactive ^{207}Bi on the edges of the PMT windows but will limit the number of PMTs that can be put in the gap. Measurements with RPL detectors during LHC run 2 have shown that PMTs situated in the gap of the JN plug are exposed to radiation levels that are 95 times smaller than the PMTs situated around the beampipe. However, in order to replace any malfunctioning or radiation damaged PMT, the work would have to be done with the JN plug removed which means that the people involved would be exposed to very large radiation levels.

If the beampipe support cone cannot be made smaller the 10 mm diameter fiber bundles will have to enter into the cone immediately after the VAX support box (see Fig. 3.14) in order to not be in conflict with the toroid shielding during YETS. This makes the situation more complicated but one could still envision having two fiber bundles above and two fiber bundles below the beampipe. They would now most likely have to be water-cooled during the beampipe bakeout and would therefore have to be attached to water-pipes.

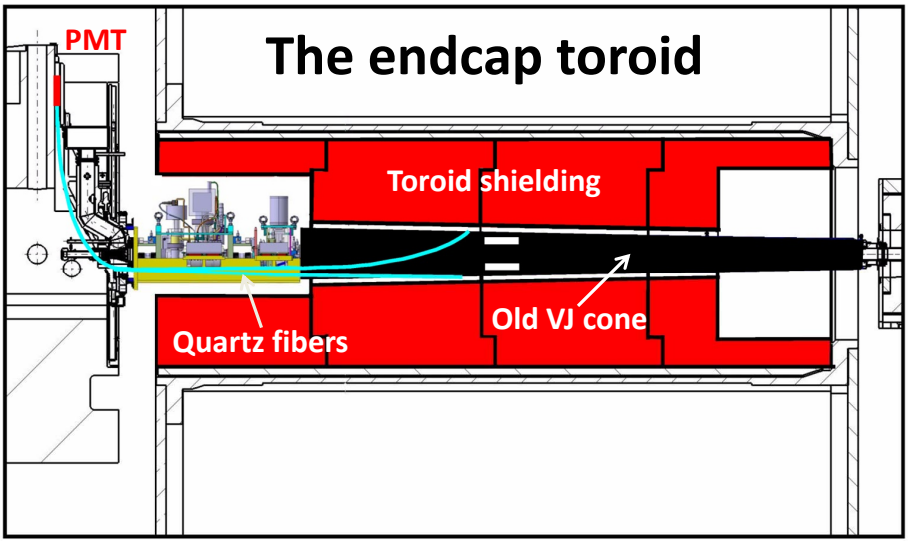

Figure 3.14: The drawing shows the location of the endcap toroid shielding in relation to a beampipe cone and a fiber detector during a standard ATLAS opening when the toroid is moved back over the beampipe until it is almost in contact with the JN shielding. The beampipe cone in this picture is the same size as the present cone.

While the gain of the photomultipliers would be monitored with radioactive ^{207}Bi sources, any deterioration of the fibers due to radiation damage would be monitored by a set of LEDs connected to the other end of the fiber bundles. These LEDs would be placed together with the PMTs in the gap between the JN plug and the JN monobloc. If it turns out that the radiation levels are too high in the gap for the LEDs, they will have to be placed in the pocket on the JN monobloc with a couple of fibers taking the light to the end of the fiber bundle. The LEDs would also be connected directly with one or several fibers to the PMTs so that the stability of the LEDs can be monitored.

3.6 LUCID-3 prototype in Run-3

The various options for a LUCID-3 detector have been discussed in the previous section. GEANT 4 simulations have been made that give predictions of the efficiency of PMTs at different locations but these predictions do not have the required accuracy to determine if hit-saturation will occur. A prototype detector of a PMT detector attached to the JFC3 shielding during LHC run 3 can measure what the efficiency of a PMT will be in the new location. The only thing such a measurement cannot predict is the effect of the VAX equipment. However, the VAX will be more than one meter behind the PMTs and the effect of back-splash from interactions in the VAX will probably be smaller than the

back-splash from the TAS collimator with LUCID-2.

The other major proposal is for a new FIBER detector. This detector would use new larger PMTs monitored by Bi-207 and a new type of radiation-hard fibers monitored by LED signals. The CHARGE method would have to be used to measure luminosity with this detector. Perhaps this CHARGE measurement can be stabilized by a raw uncorrected HIT-measurement. To test all this also a FIBER prototype detector is proposed to be installed before LHC Run-3.

Finally, there have been suggestions that perhaps a new location can be found in the shadow of the shielding that would dramatically reduce the efficiency of the detector. Simulations have shown that a detector placed on the outside of the forward shielding would have so few hits it would be useless. A PMT behind the forward shielding but close to the edge of the beampipe hole could perhaps get enough hits to provide a low-rate measurement. It is proposed that also such a detector is tested during LHC Run-3.

3.6.1 PMT detector attached to the shielding

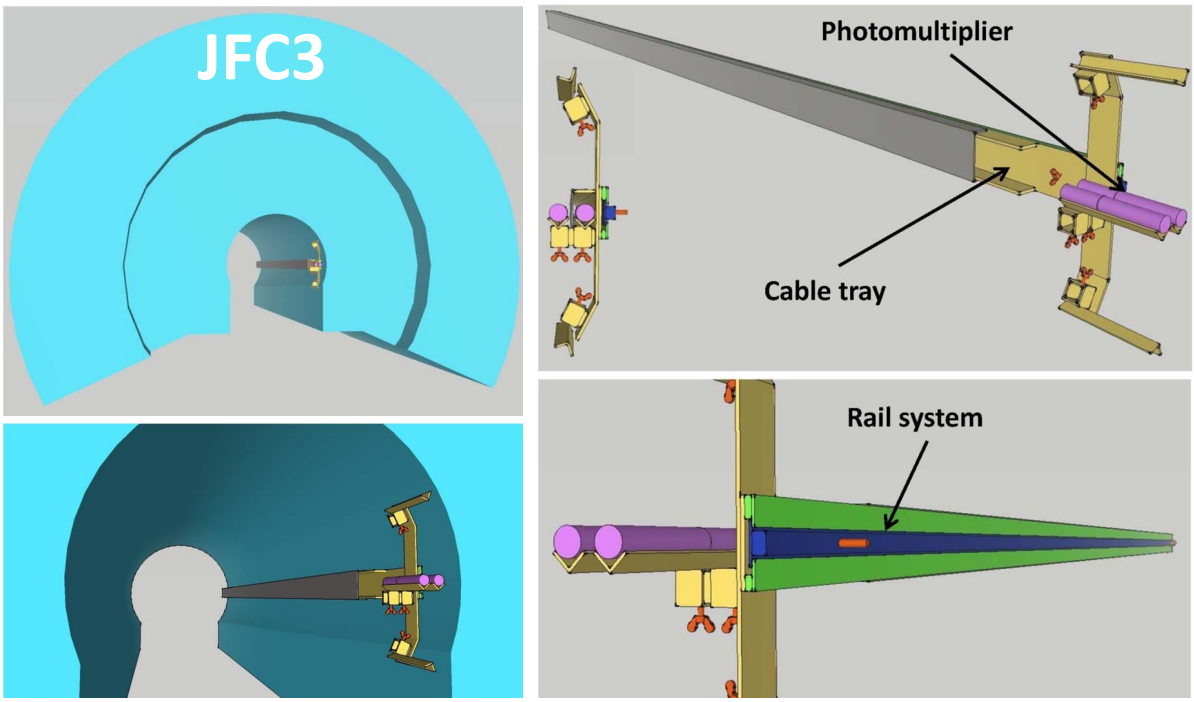

Figure 3.15: Drawings of the PMT prototype detector attached to the JFC3 forward shielding.

The prototype PMT detector that will be attached to the JFC3 shielding on the C-side is shown in Fig. 3.15. One set of two standard R760 PMTs will be attached to the

C-side shielding and another set of two new smaller R1635 PMTs will be attached to the A-side shielding. The detector will have only two + two PMTs since there are no empty read-out channels and four of the channels in the old FIBER detector will be used for the read-out. The idea is to build two of the four attachments proposed for the final detector (see Fig. 3.4) and install two PMTs in the center location on each side. The PMTs can later be moved to the top and bottom location in an YETS so that the efficiency can also be measured in this location. The rail system will be identical to that proposed for the final detector and it can thus be tried and tested already during LHC Run-3. The rail will be attached to the front and the back of the beampipe hole which requires threaded holes to be made into the ductile cast iron of the JFC3 shielding. Additional holes have to be drilled to the back-face of the shielding in order to be able to attach the services.

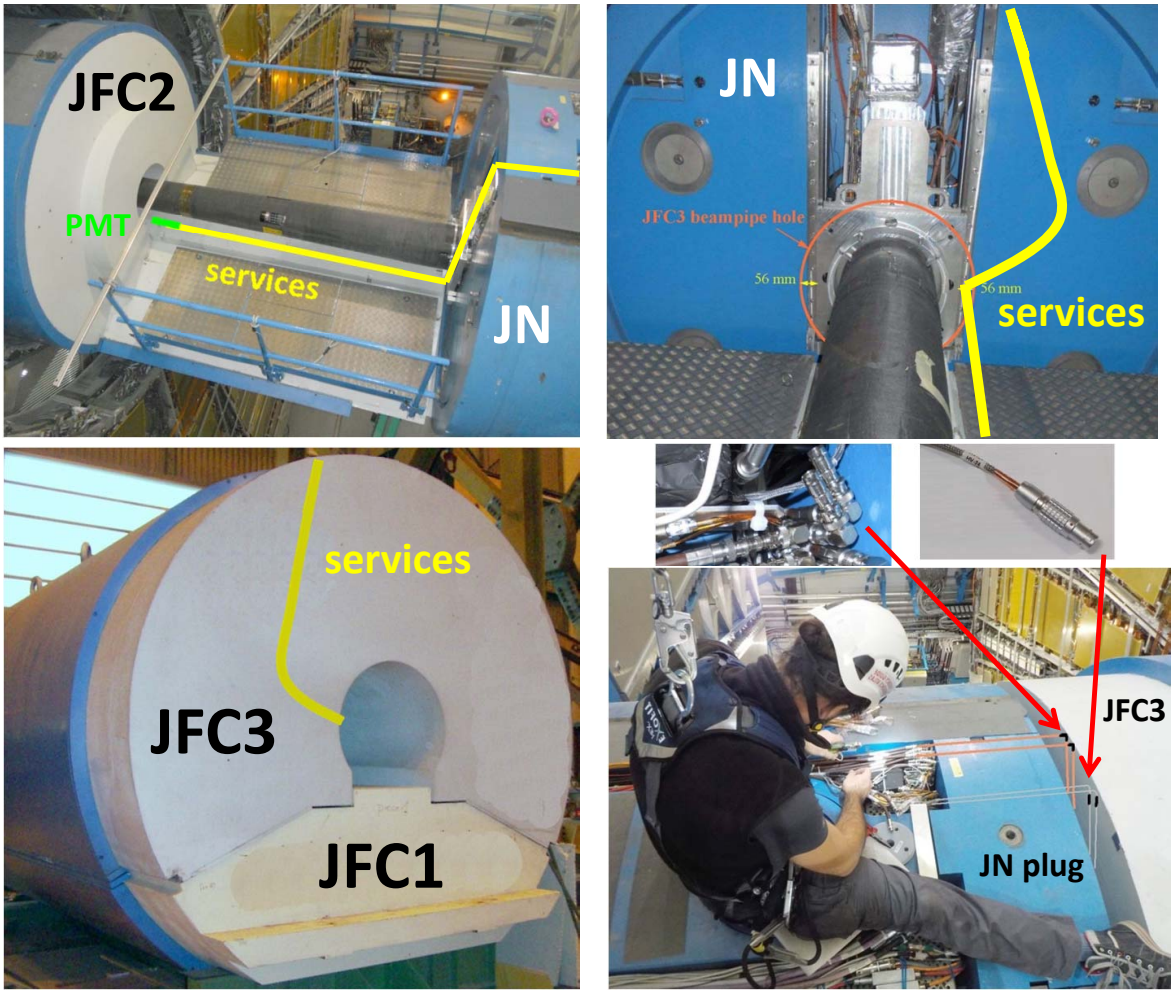

Figure 3.16: Photos on which the location of the services have been drawn for a PMT prototype detector that is attached to the JFC3.

The services will consists of two signal cables and two high voltage cables. The routing of the services is indicated in the photos in Fig. 3.16. The first part of the services runs in the cable tray that sits on the rail in the beampipe hole of the JFC3. At the end of the JFC3 the cables will have to do a 90 degree turn to the right and then go up to the top of the shielding. The signal cable is of CC50 type and is very stiff. It is therefore proposed to have 90 degree BNC connectors at this point. The cables will be attached to the back wall of the JFC3 with clips so that they can quickly be loosened during shutdowns when the detector will have to be pulled out of the beampipe hole. On top of the JFC3 shielding there will be two more 90 degree BNC connectors for the signal cables and two high voltage connectors. These four connectors will have to be disconnected and connected in every shutdown when the JFC3 is removed on side C. Finally there are some 525 mm long CC50- and HV-cables that goes over the top of the JN plug to the existing connectors that are in a pocket on top of the JN monobloc. Contrary to the final LUCID-3 detector it is not proposed to machine off the top of the JN plug for this 2-channel prototype detector.

3.6.2 Fiber detector attached to the beampipe

If the PMT detector attached to the shielding does not work well enough then a FIBER detector attached to the beampipe can be a good alternative. A two-channel prototype of such a detector on side C is also proposed to be built for LHC run 3 as described in Fig 3.17.

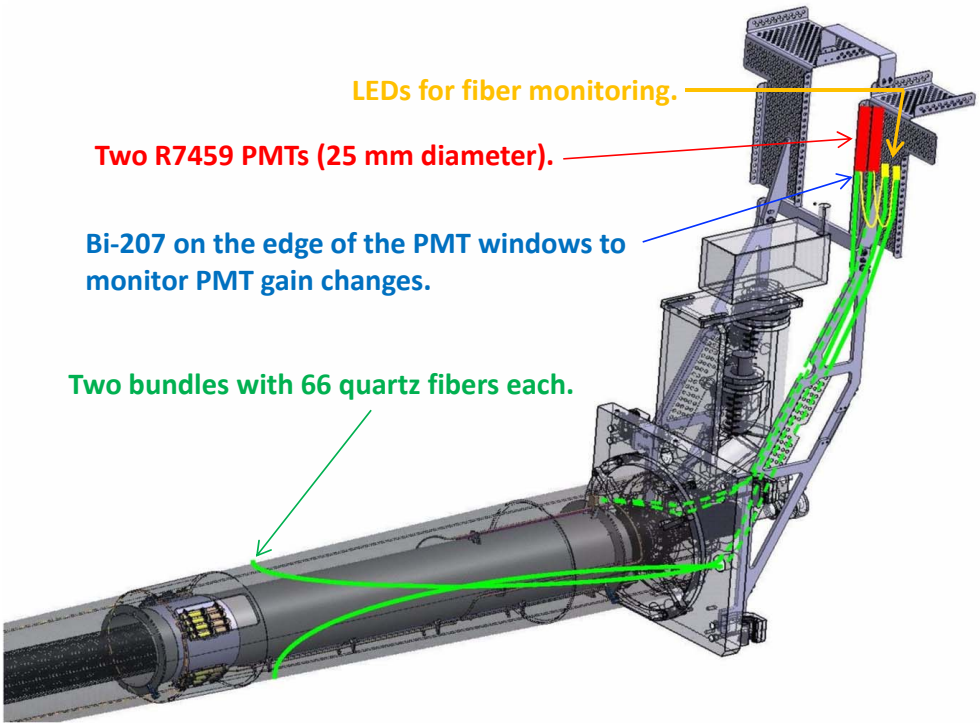

Figure 3.17: The LUCID fiber prototype detector that is planned for run 3.

The two new photomultipliers will be of the type Hamamatsu R7459 with 28 mm diameter while the quartz fibers will be of the type UVNSS 600/624/660. These fibers have a silica glass core with a diameter of 0.6 mm and a polyimide jacket that results in an outer diameter of 0.66 mm. While the old fiber bundles had 37 fibers, the new will have 66 fibers so that the total core diameter in the bundles are approximately the same.. The minimum bending radius of the new fiber will be 18 cm which makes it impossible to have the fibers going to the pocket on top of the JN monobloc.

The most important difference between the old and new fibers is the cladding. The old fibers used a silicon cladding while the new fibers have a more radiation hard Fluorine-doped silica cladding. This results in a small numerical aperture of 0.28 compared to the 0.40 of the old fibers. The change of aperture can result in less light being collected by the new fibers and this is one of the aspects that the new detector will study.

The photomultipliers would be located in the same 65 mm gap between the JN plus and the JN monobloc where the present four FIBER PMTs are located and they would replace the old PMTs. Decreasing photomultiplier gain is one of the major problems when PMTs are used to measure luminosity. While the old FIBER detector used LEDs monitored by PIN diodes to monitor and control the gain, the new detector will use radioactive Bi-207 sources, applied to the edges of the PMT windows, to monitor the gain. The old FIBER detector did not have any monitoring of any degradation of the

optical fibers while the new detector will have a set of LEDs attached to one end of the fiber bundle with a couple of fibers going directly to the PMTs. The idea is that monitoring the ratio of the amplitude of the LED signal going through the fiber bundle to the PMT with respect to the signal going directly to the PMT will give a result that can be used to monitor and correct for the fiber degradation. Several LEDs with different wavelengths make it possible to monitor any degradation as a function of the wavelength of the light. The radiation dose these LEDs will be exposed in LUC Run 3 is estimated to be about 700 Gray based on measurements in LHC Run 2 and an assumption of a total integrated luminosity of 400 fb^{-1}.

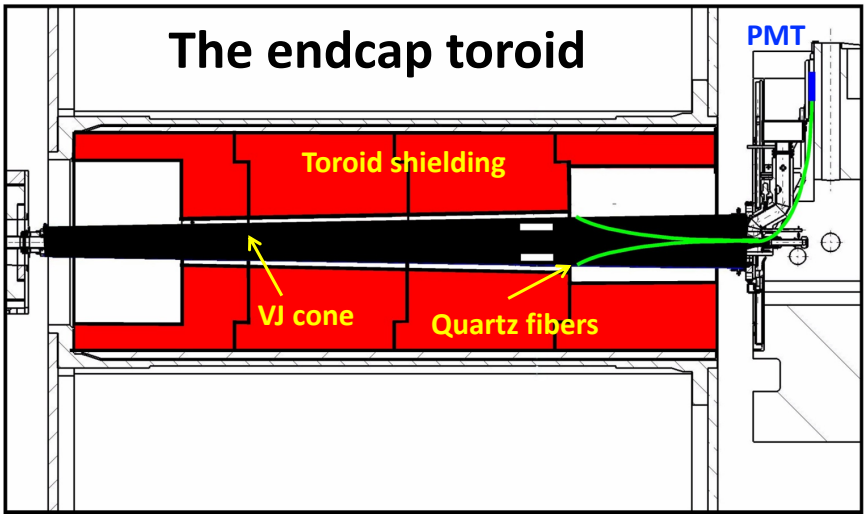

Figure 3.18: The drawing shows the location of the endcap toroid shielding in relation to the beampipe cone and the fiber detector during a standard ATLAS opening when the toroid is moved back over the beampipe until it is almost in contact with the JN shielding.

The LED signal going directly to the PMT and via the fiber bundle have to be sufficiently separated in time so that both can be measured by the same photomultipliers. For this reason the length of the fiber bundles have to be at least 6 meters. The bundles will go through two holes that already exist in the VJ cone backplate as depicted in Fig 3.19. One bundle would go over the top and another over the bottom of the VJ cone and they would be place in copper tubes so that they are mechanically protected. The clearance of these fiber bundles to the forward shielding does not seem to be a problem as can be seen in the drawing in 3.19.

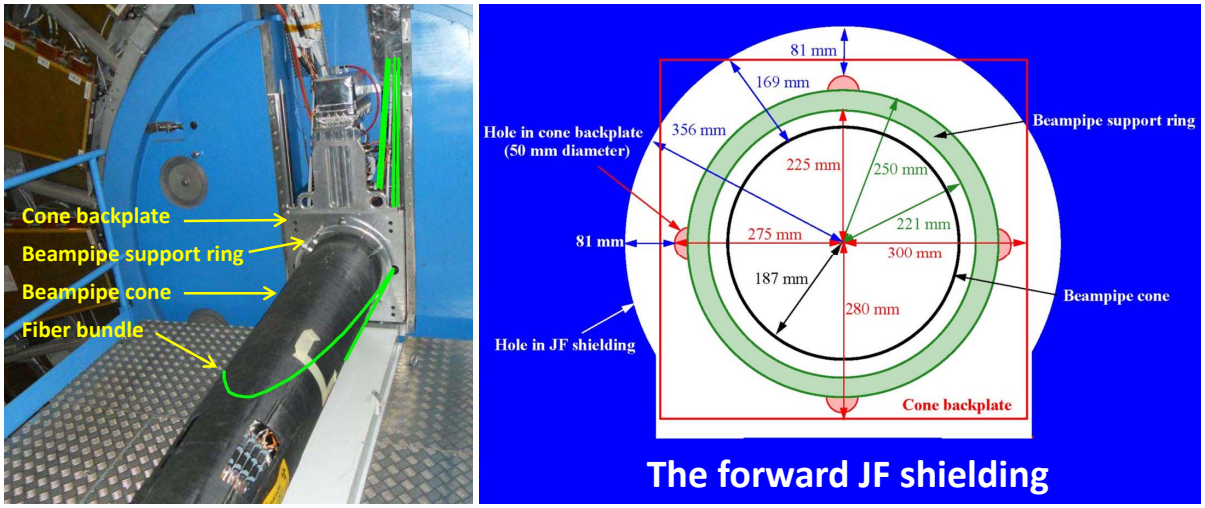

Figure 3.19: The left photo shows the VJ cone, with its backplate and support ring. The new fiber bundles will go through holes in the backplate as indicated in the photo. The drawing on the right shows the dimensions of the backplate with its holes in relation to the forward shielding when that is fully installed.

As discussed before, the clearence of the fiber bundles to the toroid shielding would be a problem only for LUCID-3 FIBER detector because VAX won't be present during Run-3.

3.6.3 Fiber detector stability monitoring

Due to the local and direction nature of the light produced in the fibers and the different local nature of the irradiation and consequent opacification, the fiber calibration is not just a matter of using the LED light to generate a linear correction of the measured charge. Two main factors come into this computation:

- the opacification is not the same for all light wavelengths, with a distribution that varies with time and fiber material used;
- the LED light experiences losses over the whole length of the fiber, while the collision light experiences a smaller loss that depends on the distribution of the light produced and of the opacification;

To face these two complications several measurements and simulations are needed:

- the opacification dependence on wavelength and irradiation will be measured in a dedicated gamma irradiation test using 6 different wavelengths (280-630 nm), followed by an additional measurement performed with a Xenon lamp and a wavelength selector, in order to investigate a more continuous spectrum;

- during the calibration runs in ATLAS, 6 different wavelength LED's will be used, one at a time, to pulse light into the bundles and into a shorter control fiber; the variation in time of the ratio between these two signals provides a measurement of the integrated opacification;
- the spatial and wavelength distribution of the light produced in the fiber during collisions is going to be simulated and used as an essential input for the calibration algorithm;
- the spatial distribution of the dose absorbed by the fiber needs be simulated as the final input to the calibration program.

In this way the calibration LED light can be used to scale the wavelength-dependent opacification distribution measured in lab and irradiation tests. The simulation of the wavelength distribution is then convoluted with the normalized quantum efficiency of the PMT to obtain the input light without opacification. For each bin in this distribution, the spatial distribution comes into play, determining how much light is absorbed from the production point to the PMT, using the opacification of each specific wavelength bin.

3.6.4 Low rate PMT detector behind the shielding

It is not clear if the reduction of the particle flux when going from the VJ cone to the wall of the JFC3 will be enough to allow for the use of standard PMTs and so a suggestion has been made that one could put the PMTs behind the forward shielding. In this way one could possibly reduce the HIT-rate in the PMTs to any level. GEANT4 simulations have shown that PMTs installed outside of the forward shielding would have a far too low HIT-rate and so the proposal has been to install two PMTs as shown in Fig. 3.20.

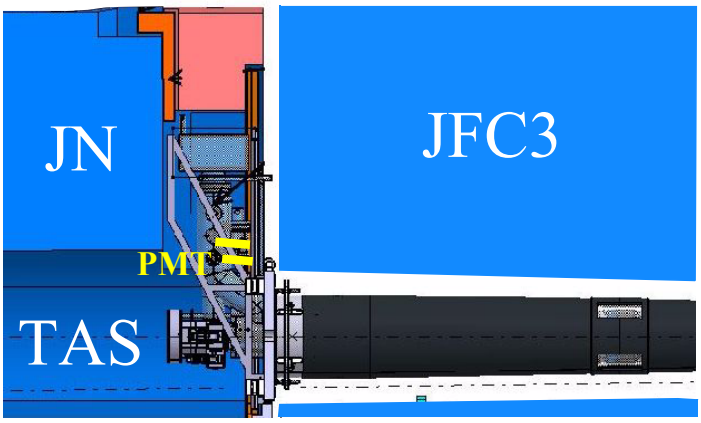

Figure 3.20: The drawing show a sideview of low-rate PMT prototype detector that is located behind the forward shielding and the photo to the right illustrates where the photomultipliers would be attached (in yellow).

According to the GEANT4 simulations the rate at the back of the JFC3 shielding will be reduced quickly as a function of distance to the beamline. It is therefore important to locate the new photomultipliers close to the edge of the beampipe hole in the JFC3 shielding. A location 1-2 cm above the beampipe hole would see only 15-30% of the HIT-rate observed for LUCID-2. At a distance larger than 3 cm the rate would be less than 10% of the rate in LUCID-2. A reduction of 15-30% should be enough to not saturate luminosity algorithms.

A difficulty with this detector will therefore be to find the right location so that the HIT-rate will not be small. The proposal is to put two of the new Bi-207 calibrated PMTs on top of each other on side A as shown in Fig. 3.21 and Fig. 3.22. The read-out of two of the old FIBER detector channels would be used for the new detector. The main work needed to implement this prototype detector will be to make new high voltage cables that can support both two of the old FIBER detector channels and the two new PMT channels. The bases on the old FIBER detector will either have to be changed or new HV connectors will have to be added to the old detector channels.

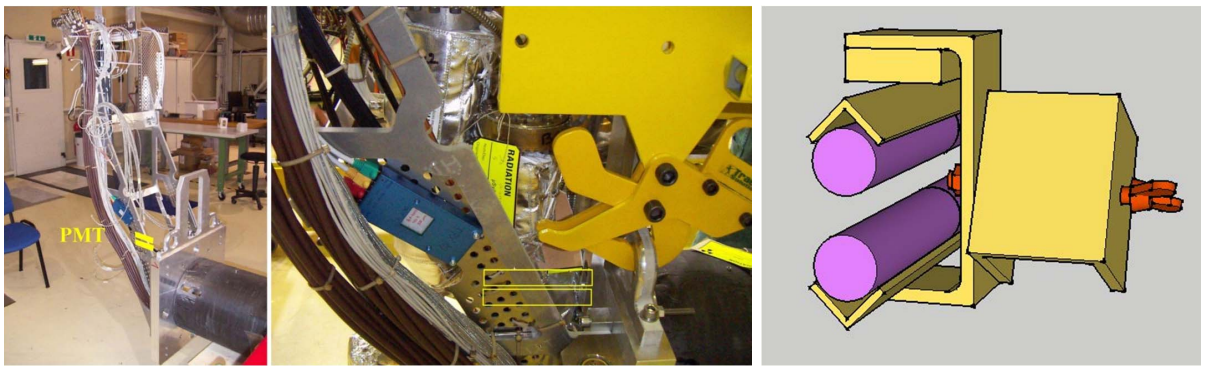

Figure 3.21: Photos that indicate where the photomultipliers will be attached (yellow rectangles) in the low-rate PMT prototype detector in order for the photomultipliers to be behind the forward shielding. The drawing to the right shows the attachment mechanism.

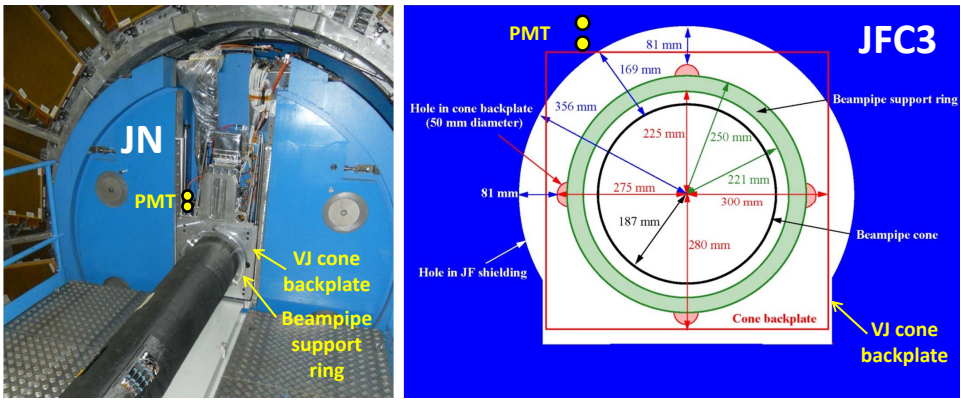

Figure 3.22: The photo on the left shows where the photomultipliers would be located. The drawing on the right shows where the photomultipliers would be located in relation to the forward shielding after the top piece of the shielding has been installed.

Chapter 4

Fiber irradiation campaign

4.1 Introduction

Since one of the prototypes of LUCID-3 is based on fiber, it's important to understand how the fibers behave when irradiated. To do so, a session of a γ-irradiation was performed using the Calliope facility at ENEA. Before discussing the results, it will be explained how the experimental setup is made and what preliminary test were made and their result.

4.2 Experimental setup

The purpose of this experiment is to study how the light transmission inside the fiber varies as a function of the wavelength and the absorbed dose. To do so, the experimental setup must be able to take data also during the irradiation. Thus, it can be divided into two parts: one of them would stay near the γ source and the second one would stay in a radiation free area.

The first one is made of 3 quartz fiber (model UVNSS600/624/660, 2 of them with a numeric aperture of 0.28 and the last one with a numeric aperture of 0.22), 4 LEDs with different wavelength (MTE280F13-UV ($\lambda = 280nm$), MTE340H21 ($\lambda = 340nm$), VCC VAOL-5GUV8T4 ($\lambda = 385nm$), LEDRGBE (RGB LED $\lambda = 627.5, 525, 467.5nm$)), 2 pin diodes and 2 distribution boxes. One distribution box(the gray one) takes the light from the LEDs and connects it to the fibers and to one pin-diode to monitor the stability of the LEDs (we will refer to this pin-diode as LED-pin-diode). The second distribution box is attached to the other end of the fibers and merges the light from the fibers to the other pin-diode (we will refer to this pin-diode as fiber-pin-diode) (Fig 4.1). Out of the 3 fibers, only the ones with a numerical aperture of 0.28 will be read while the last one is only irradiated and will be studied later to see if there is a difference in the light transmission with respect to the other 2.

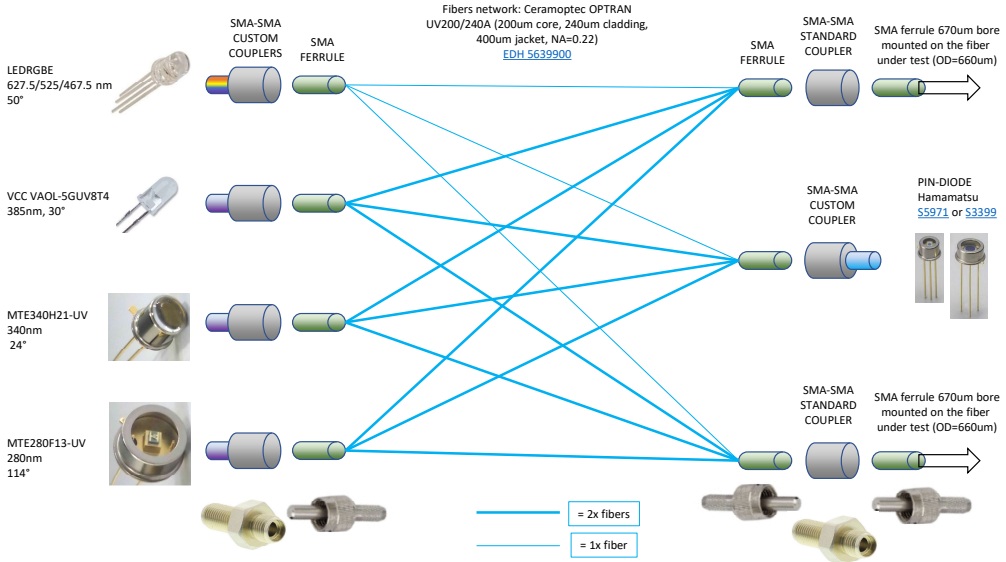

(a) Scheme of the silver box

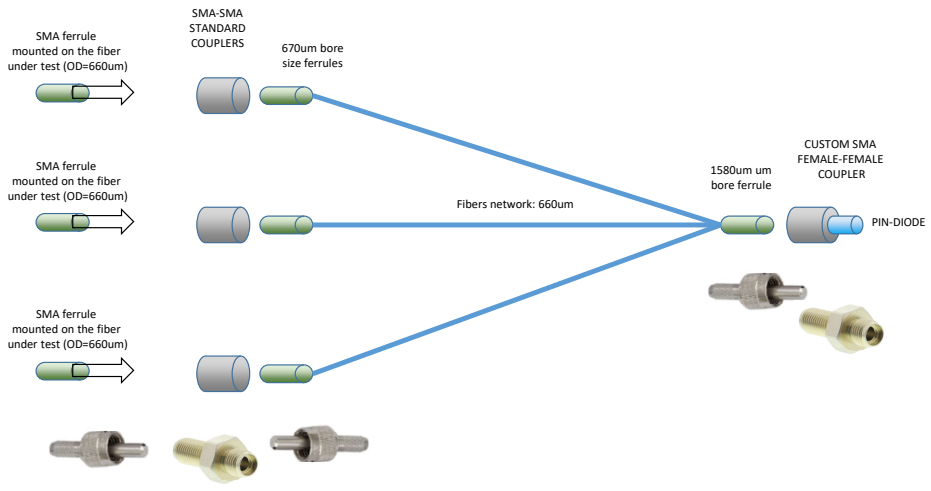

(b) Scheme of the black box

Figure 4.1: Scheme of the two distribution boxes

The second part of the system consists of a picoammeter (Keithley 6485), a sourcemeter (Keithley 2410), an arduino UNO board, a power distribution circuit and a PC. Since the sourcemeter is less sensitive than the picoammeter, it was selected to read the LED-pin-diode since the light it receives is not expected to decrease during irradiation. The picoammeter will, instead, read the fiber-pin-diode. The PC controls the picoammeter, the sourcemeter and the Arduino board through a python program that uses the pyfirmata and Tektronic libraries. The Arduino board is programmed using with the Firmata protocol for serial remote port control and is connected with a 25m 4-wire cable to the power distribution circuit piloting the LED's. Using the python program, we cycle on the LED in order to turn on only one LED each time. The cycle also contains one iteration where all the LEDs are off in order to control the background. The Arduino UNO board is only able to provide 5V as output tension. None of the LEDs that were used has a nominal tension of 5V so a power distribution circuit must be done (Fig 4.2). One of the main requirement of the circuit is to keep the number of cables as low as possible. For this purpose, the same power supply was used both for a component of the RGB LED and for one of the other LEDs. Placing the 2 "paired" LED with opposite polarization, we are able to turn on only one LED and, by inverting the role of the ground and the power supply, we turn on the other one. Since each LED has a different operating voltage, some resistors were put inside the circuit. For the 280 LED, the nominal tension is 7V. This could have been a problem but it's clear from the tests that were made that also 5V are enough to power the LED. The 340 LED and 385 LED have the same nominal tension of about 4V so two resistor of 220 Ω were used. RGB LED has a nominal tension of 3.2 V so a resistor of 560 Ω was used.

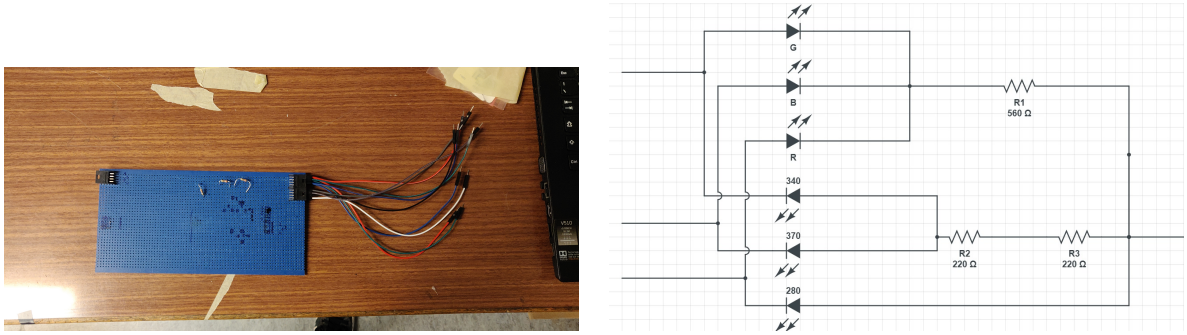

(a) (b)

Figure 4.2: Photo and scheme of the distribution circuit

There are several challenges that need to be addressed with this setup. First of all, the total dose integrated over the length of the fiber needs to be extrapolated from the information provided by the irradiation facilities. Secondly, the UV LEDs emits visible lights so it's important to separate the visible component from the UV component. These

two points are discussed in the following chapters. Another potential challenge is the non-flat quantum efficiency of the pin diodes. This is solved by using two identical PIN Diode models and by looking at the variation as a function of the dose (or of time) of the ratios between the LED-pin-diode and the fiber-pin-diode.

4.3 LED preliminary test

As alredy mentioned, the degradation of the fibers depends from the wavelength of the light. To study this dependence, 4 different LEDs were used. Since the LEDs are not perfectly monochromatic, some test were performed to evaluate the UV component and the visible component for each LED.

The tests consist in monitoring the LEDs light with a pin-diode in various condition:

- without any filter: we will see all the light produced by the LED
- with a visible filter: we will see mostly the visible component and only a minimal part of UV component
- with a UV filter: we will see mostly the UV component and only a minimal part of visible component
- with both filter: we will see only the fraction of the light that constitutes a cross contamination between the UV and visible wavelengths.

For each LED, we can write the following equations:

$$L = UV + VIS \tag{4.1}$$

$$L_{vis} = \epsilon_{vis}^{vis} VIS + \epsilon_{UV}^{vis} UV \tag{4.2}$$

$$L_{UV} = \epsilon_{vis}^{UV} VIS + \epsilon_{UV}^{UV} UV \tag{4.3}$$

$$L_{double} = \epsilon_{vis}^{vis}\epsilon_{vis}^{UV} VIS + \epsilon_{UV}^{vis}\epsilon_{UV}^{UV} UV \tag{4.4}$$

L is the light that we see when we use no filter, L_{vis} is the light that we see when we use the visible filter, L_{UV} is the light that we see when we use the UV filter, L_{double} is the light that we see when we use the visible filter. ϵ_{vis}^{vis} is the fraction of visible light that pass through the visible filter, ϵ_{UV}^{vis} is the fraction of UV light that pass through the visible filter, ϵ_{vis}^{UV} is the fraction of visible light that pass through the UV filter, ϵ_{UV}^{UV} is the fraction of UV light that pass through the UV filter. UV and VIS are the UV and visible component of the LED light. We expect to have $\epsilon_{vis}^{vis} \approx \epsilon_{UV}^{UV} \approx 1$ and $\epsilon_{UV}^{vis} \approx \epsilon_{vis}^{UV} \approx 0$.

As we will see later, for the RGB LED we can consider $UV = 0$. Therefore the previous equations can be written as:

$$L = VIS \tag{4.5}$$

$$L_{vis} = \epsilon_{vis}^{vis} VIS \tag{4.6}$$

$$L_{UV} = \epsilon_{vis}^{UV} VIS \tag{4.7}$$

$$L_{double} = \epsilon_{vis}^{vis} \epsilon_{vis}^{UV} VIS \tag{4.8}$$

Thus, we are able to measure ϵ_{vis}^{vis} and ϵ_{vis}^{UV}. These $\epsilon$are determined only by the filters, bit by a specific LED, so the value that we have obtained can be used for all the other LEDs.

For the other LEDs we have a system of 4 equations and 4 unknown variables which can be solved. From eq 4.1, we obtain

$$VIS = L - UV \tag{4.9}$$

From eqs 4.2 and 4.3 we can obtain ϵ_{UV}^{vis} and ϵ_{UV}^{UV}

$$\epsilon_{UV}^{vis} = \frac{L_{vis} - \epsilon_{vis}^{vis} VIS}{UV} \tag{4.10}$$

$$\epsilon_{UV}^{UV} = \frac{L_{UV} - \epsilon_{vis}^{UV} VIS}{UV} \tag{4.11}$$

Substituting these equation in eq 4.4 the only unknown parameter is UV. UV can be expressed as:

$$UV = -\frac{L_{vis} L_{UV} + L L_{vis} \epsilon_{vis}^{UV} - L L_{UV} \epsilon_{vis}^{vis} + L^2 \epsilon_{vis}^{vis} \epsilon_{vis}^{UV}}{-L_{double} + L \epsilon_{vis}^{vis} \epsilon_{vis}^{UV} + L_{vis} \epsilon_{vis}^{UV} + L_{UV} \epsilon_{vis}^{vis} - 2L \epsilon_{vis}^{vis} \epsilon_{vis}^{UV}} \tag{4.12}$$

Once we know the value of UV for each LED, we can substitute it into eq 4.9 and obtain VIS.

During these test, the current inside the LED may not be stable, especially if the temperature of the LED itself changes. An instability in the current inside the LED leads to an instability of the light emitted. This won't be a problem during the irradiation since we monitor the LED using the sourcemeter and, dividing the picoammeter signal by the sourcemeter signal, we cancel off the LED intrinsic instability.

4.4 Effect of the irradiation

The light absorption effect due to opacification is exponential as a function of the length the light travels within the fiber. Since we have the LEDs at one end and the sensor at the opposite end, we can only observe a compound effect that is independent from the topology of the opacification effect. Nonetheless, a map of the irradiation is necessary to calculate the total dose and could be extremely useful in future studies.

4.4.1 Dose Absorbed by the Fiber

For a point-like γ ray source, we know that the emission is isotropic so the energy flux $\phi(r)$ can be written as:

$$\phi(r) = \frac{E_0}{4\pi r^2} \cdot e^{-\lambda r} \tag{4.13}$$

where E_0 is the total energy emitted that is not known a priori, r is the distance from the source and λ is linear attenuation coefficient. If we want to know how much energy the fiber absorbs we must introduce the mass energy transfer coefficient $\left(\frac{\mu}{\rho}\right)_{E,Z}$ which depends on the energy of the photons E and the Z of the material. We can now calculate the kerma K as[18]:

$$K = \phi \cdot \left(\frac{\mu}{\rho}\right)_{E,Z} \tag{4.14}$$

if the photons are mono-energetic. Since we have rods of radioactive source, and therefore an extended source, we can consider the rods as an ensemble of point-like sources. If the kerma and the absorbed dose are the same we can calculate the absorbed dose (D) in a point as:

$$D = \int_0^L \frac{E_0}{L} \frac{e^{-\lambda\sqrt{((x_p-x_s)^2+(y_p-y_s)^2+(z_p-(z_s+l))^2)}}}{4\pi((x_p-x_s)^2+(y_p-y_s)^2+(z_p-(z_s+l))^2)} \left(\frac{\mu}{\rho}\right)_{E,Z} dl \tag{4.15}$$

where L is the length of the rod, x_p, y_p, z_p are the coordinate of the point we are interested in, x_s, y_s, z_s are the coordinate of the lowest end of the rod. Since E_0, L, 4π and $\left(\frac{\mu}{\rho}\right)_{E,Z}$ are constant we can bring them out of the integral and for simplicity we can define k as

$$k = \frac{E_0}{L} \frac{1}{4\pi} \frac{\mu}{\rho}_{E,Z} \tag{4.16}$$

It is straightforward to generalize this formula in the case of multiple rods (in this case Calliope has 25 rods). In fact, the total dose is just the sum of the single doses. Since k and λ are unknown we can determine their value from the dosimeters that are placed during the irradiation. k and λ are considered constant for all the duration of the irradiation unless otherwise noted. We know this because this was measured by the irradiation facility, showing a $< 0.1\%$ reduction in dose from beginning to end of the irradiation. The doses are measured in silicon-equivalent dose. We irradiated a quartz fiber so we consider the conversion coefficient equal to 1.

The absorbed energy is

$$E_{abs} = \int_V D\rho dV \tag{4.17}$$

where V is the volume of the material and ρ is its density. We can therefore calculate the energy absorbed by the fiber as

$$E_{abs} = k \int_V \int_0^L \frac{e^{-\lambda\sqrt{((x_p-x_s)^2+(y_p-y_s)^2+(z_p-(z_s+l))^2)}}}{((x_p-x_s)^2+(y_p-y_s)^2+(z_p-(z_s+l))^2)} \rho dl dV \tag{4.18}$$

As before, to calculate the total absorbed energy we can just sum all the contributions for each rod. Now we can work on the effect of the absorbed energy on the transmission of light.

The program for the extrapolation and the integration of the radiation is based on the framework ROOT v6.24. All the integrals were performed using the class AdaptiveIntegratorMultiDim with a relative tolerance of 0.001. To calculate the dose absorbed by the fiber, the fiber is divided into 3 pieces: 2 cylindrical parts parallel to the source rack and one toroidal part that connects the two cylinders.

4.4.2 Effect of the radiation on the fiber

We need now to study the behavior of the fiber when irradiated. If we consider a slab of material of thickness dx we know that

$$dI = -\mu I dx \tag{4.19}$$

where I is the intensity of the light and μ is the absorption coefficient. Because of the irradiation, the fiber degrades so μ can change. We can make an ansatz:

$$\mu = \mu_0(1 + m\frac{dE}{dx}(x)) \tag{4.20}$$

where μ_0 is the original absorption coefficient, $\frac{dE}{dx}$ is the amount of energy that has been absorbed by the fiber in the point x and m is a constant that must be determined. We thus obtain

$$\frac{dI}{I} = (-\mu_0 - \mu_0 m\frac{dE}{dx})dx \tag{4.21}$$

Let's now suppose to divide the fiber lengthwise into many small pieces. In this case each piece can be considered as the light source for the following piece. If these pieces are small enough, we can consider the energy deposited in each piece constant so the energy deposited for unit path length can be written as:

$$\frac{dE}{dx} = \frac{E}{L} \tag{4.22}$$

where E is the energy deposited and L is the length of the piece. If we divide the fiber into pieces with equal length we obtain:

$$\begin{aligned} &I_1(L) = I_0 e^{-\mu_0 L - \mu_0 m E_1} \\ &I_2(L) = I_1(L) e^{-\mu_0 L - \mu_0 m E_2} = I_0 e^{-2L\mu_0 - \mu_0 m(E_1+E_2)} \\ &\vdots \\ &I_n(L) = I_{n-1}(L) e^{-\mu_0 L - \mu_0 m E_n} = I_0 e^{-nL\mu_0 - \mu_0 m(\sum_n E_n)}. \end{aligned} \tag{4.23}$$

The outgoing light intensity will be:

$$I_f(L) = I_0 e^{-\mu_0 L_{tot} - \mu_0 m E_{tot}} \tag{4.24}$$

It's important to notice that μ_0 and k can be wavelength-dependent. μ_0 is also provided by the fiber manufacturer and it is a very small number. The first part of the exponent in 4.24 can be omitted and it gets cancelled anyway when normalising plots to the non-irradiated ratios. The relevant quantity thus becomes the product $k\mu_0$ that can be extrapolated from fits of the signal degradation functions.

4.5 Results

4.5.1 Irradiation map extrapolation and absorbed energy

The Calliope plant[19] is a pool-type irradiation facility equipped with a ^{60}Co (mean energy 1.25 MeV) radio-isotopic source array in a high volume shielded cell. The source rack has a plane geometry with 25 ^{60}Co source rods. Two steps are necessary to extrapolate the dose.

Distance from A (cm)	Dose rate (Gy/h)
2	7700
7	5800
12	4500
17	3700
24	2700
34	2000
40	1800
44	1100
54	780
77	440
99	240

Table 4.1: Dose rate at Calliope in November 2020. The dose rate are measured in Si equivalent dose rate.

The first step uses the data obtained in November 2020 and resumed in the table (Tab 4.1). The distance is measured from the center of the source rack and along the center of the platform (see fig 4.3).

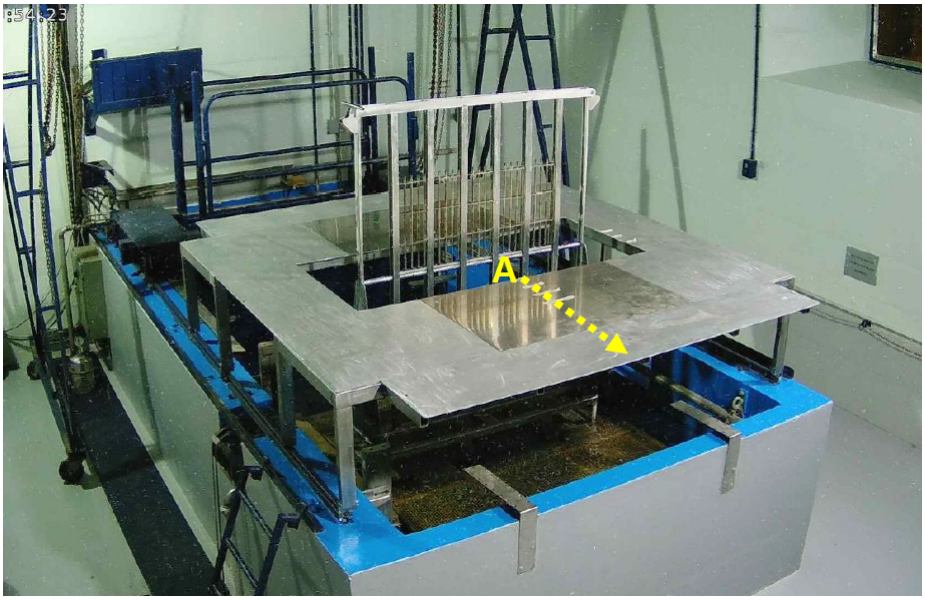

Figure 4.3: Photo of the Calliope platform

This set of data was used to test different ansatz for the radiation map. The best model is the one explained before. Via a fit k and λ were calculated and their value are 26.7 ± 2.0 and -0.88 ± 0.27. One would expect a value for $\lambda \ll 1$. This, in combination with a gap could lead to negative value for λ. In figure 4.4 is reported the profile of the dose rate as function of the distance from the source rack along A and the fit. These data are old so the parameters that depend on the activity of the source cannot be used for the irradiation. In this model, only k depends on the activity of the source (is proportional to the activity of the source) while λ is independent since is an attenuation parameter. For this reason, the value of λ just measured is kept also for the following part.

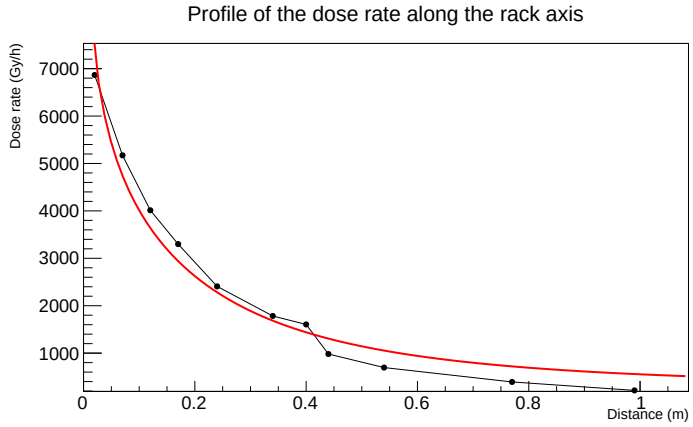

Figure 4.4: Profile dose rate along the rack axis as function of the distance from the rack

Dosimeter	Dose rate (kGy/h)
1	0.40
2	3.11
3	3.10
4	0.27
5	2.11
6	2.47
7	1.78

Table 4.2: Dose rate at Calliope during irradiation. The dose rate are measured in H_2O equivalent dose rate.

To determine k, 6 dosimeters were placed near the fiber during the irradiation. The measurements are resumed in the table 4.2. In fig 4.5 is reported the position of the dosimeter during irradiation.

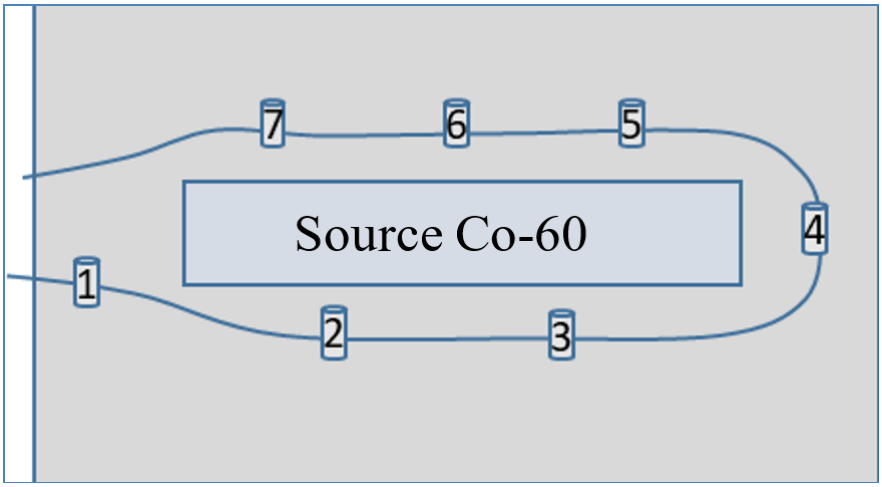

Figure 4.5: Scheme of the position of the dosimeters during the irradiation

In Fig 4.5 is reported the position of the fiber during the first part of the irradiation. In fact, from the dosimeters measurements, it was clear that in 1 week the integrated dose wouldn't have reached the expected value of 1 MGy. In order to maximize the dose, the fiber was moved closer to the rack after 65 hours and 40 min of irradiation. The first position can be schematized as: 2 parallel cylindrical parts whose length is 183.5 cm and parallel to the source rack, the left one is distant 12 cm from the left inner edge while the right one is distant 7 cm from the right inner edge. The last part is a semi-toroidal part that connects the 2 cylindrical one and its maximum distant from the inner edge is 10 cm. The second position can be schematized as: 2 parallel cylindrical parts whose

length is 196 cm and parallel to the source rack, their position is symmetric with respect to the source rack and are placed near the inner edge. The semi-toroidal part connects the two cylindrical ones and the maximum distance from the inner edge is 13 cm (fig 4.6). Despite this, the total dose hadn't reached 1 MGy but only 704.06 KGy according to the ENEA irradiation certificate.

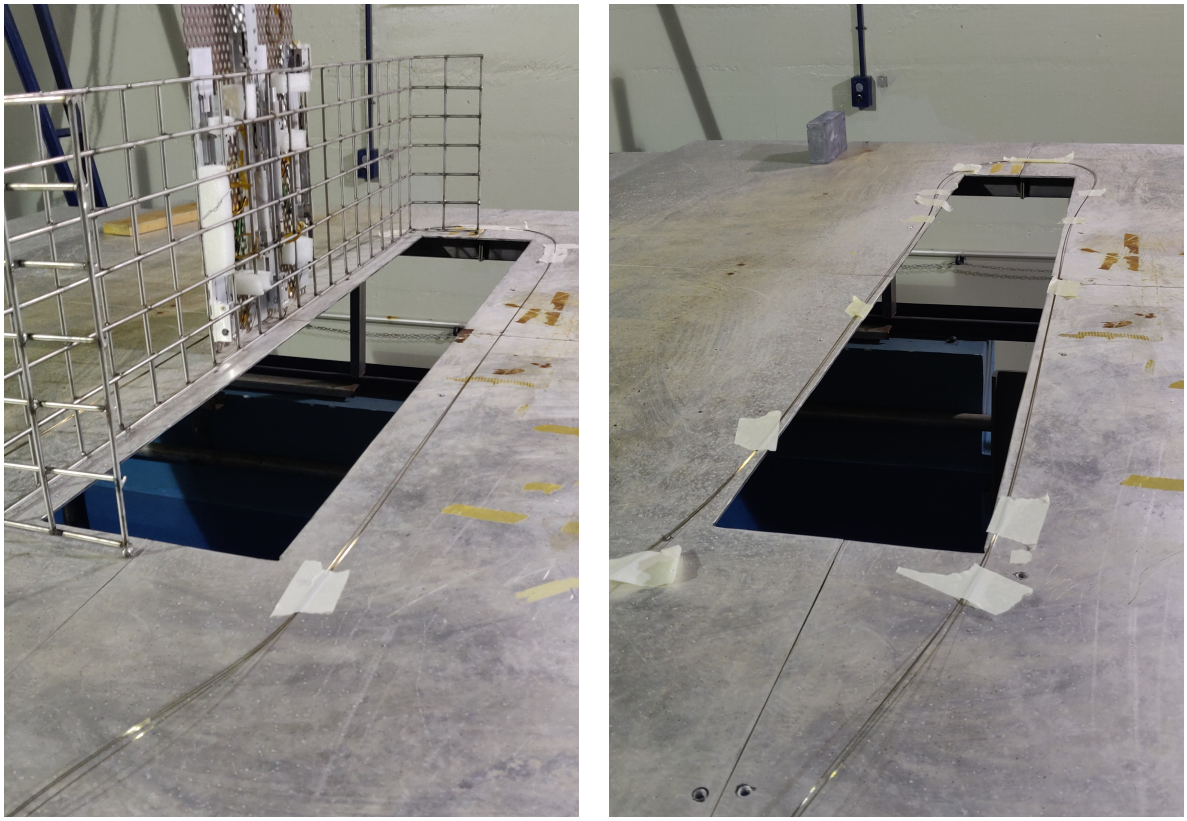

(a) (b)

Figure 4.6: Position of the fiber at the start and the end of the irradiation session

Since the dosimeter 6 in Fig 4.5 is placed in the middle and 12 away from the inner edge and the profile of the dose rate along the rack axis is known, it's possible to extrapolate the dose rate in the position of the dosimeter and then rescaling it's possible to determine the dose rate in every position of the platform. Doing this, the value of k is found to be 23.8 ± 1.8. In Fig 4.7 is reported the map of the dose rate on the Calliope table.

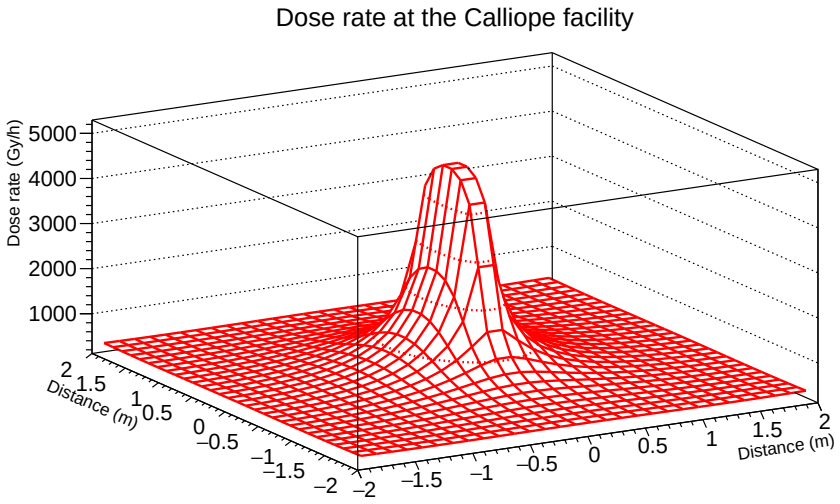

Figure 4.7: Map of the dose rate on the Calliope platform

The power absorbed by the fiber is $4.85J/h$ for the first position of the fiber and $6.48J/h$ for the second position of the fiber.

4.5.2 LED Tests

As explained, these tests consist in measuring the light emitted by the LEDs using a PIN-diode when:

- there is a UV filter ($230 < \lambda < 400nm$) between LED and PIN-diode
- there is a visible filter ($\lambda > 450$) between LED and PIN-diode
- there are both filters
- there are no filters

During these tests, the power supply voltage was modified in order to study the light output as a function of the voltage (changing the voltage, the current inside the LED changes and also the light output changes since the light output is proportional to the current).

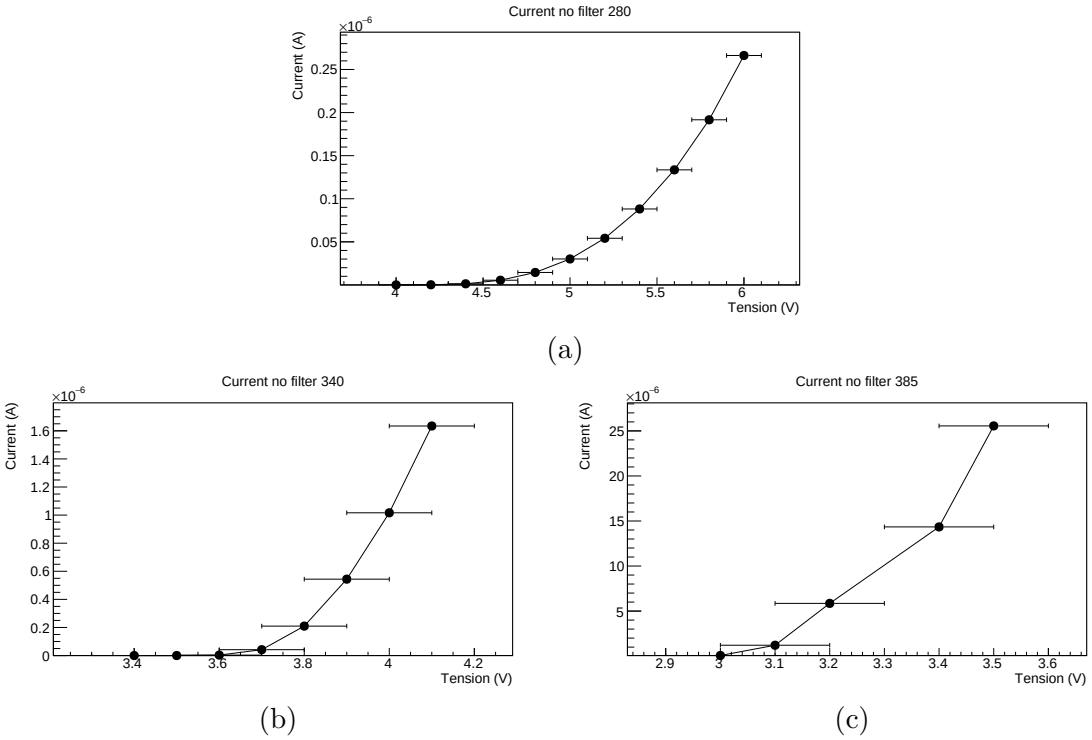

Figure 4.8: Current inside the PIN-diode as function of the tension of the LED for 280, 340 and 385 LEDs

Fig 4.8 shows that the light output has an exponential behavior with respect to the tension for all the LEDs. Dividing the current measured where there is a filter or there are both filters by the current with no filter eventual changes in the emission spectra can be spotted.

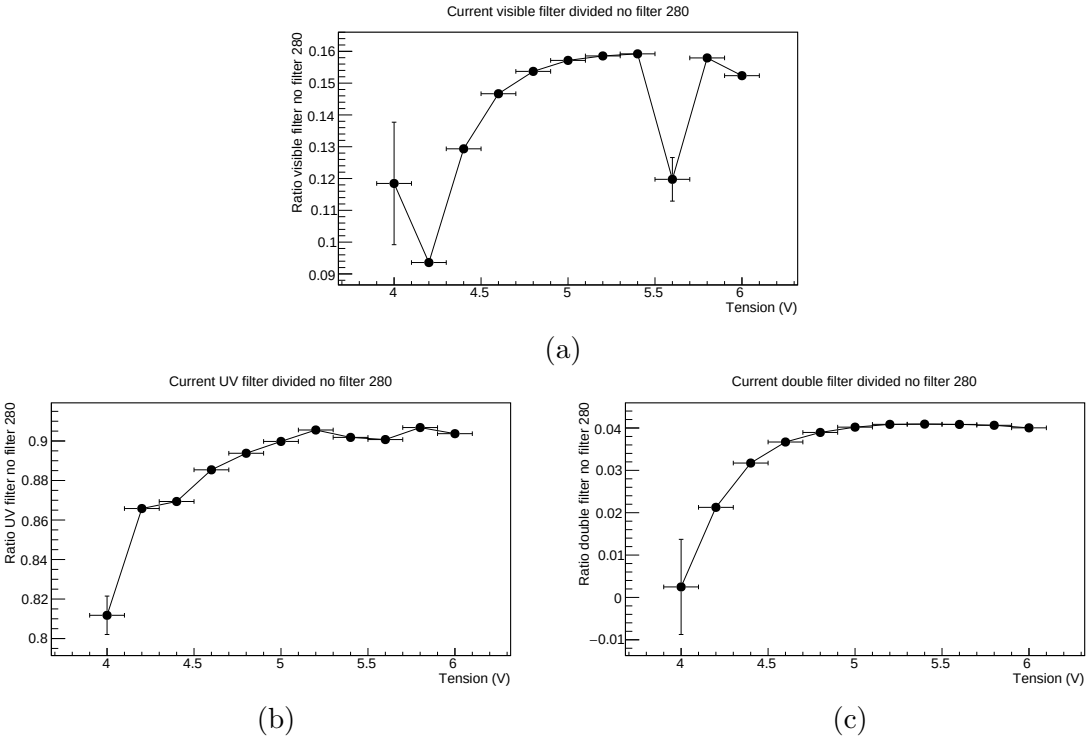

Figure 4.9: Ratio between the various combinations of the filters over no filter as function of the LED tension for 280 LED

It's clear that there is an increase in the current both in the UV component and visible component when the voltage increases. It has been observed in the literature that defects in the semiconductor structure of the LED can be excited by the UV emission and emit long lifetime (ms) light at visible wavelengths[20]. For tension that are greater than 5 V there is a plateau. This means that the fractions $\frac{UV}{L}$ and $\frac{vis}{L}$ remain constant in a good approximation.

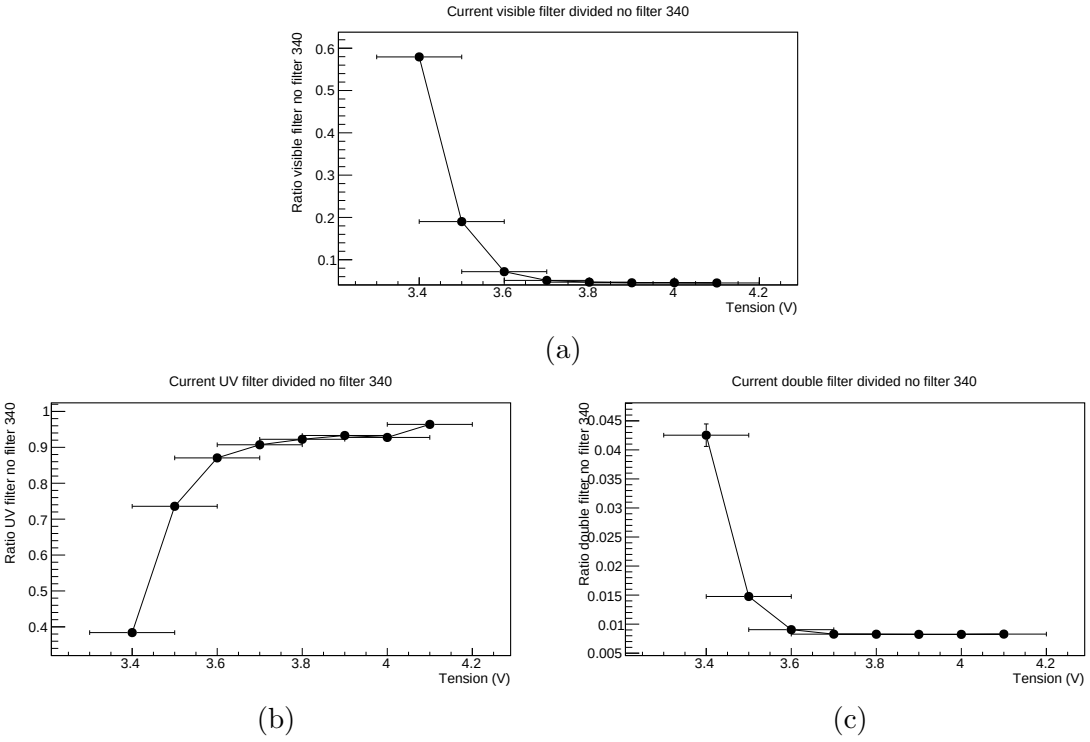

Figure 4.10: Ratio between the various combinations of the filters over no filter as function of the LED tension for 340 LED

For the 340 LED there is a decrease in the fraction of the visible component when the voltage increase and therefore there is an increase of the UV component. This is good for our experiment because we go to $\frac{vis}{L} < 0.1$ at 4V from $\frac{vis}{L} \approx 0.6$ at 3.4 V and from $\frac{UV}{L} \approx 0.4$ at 3.4 V to $\frac{UV}{L} \approx 0.9$ at 4 V. During the irradiation, the voltage of this LED is $\approx 4V$ so the UV light is the dominant component of the light emitted.

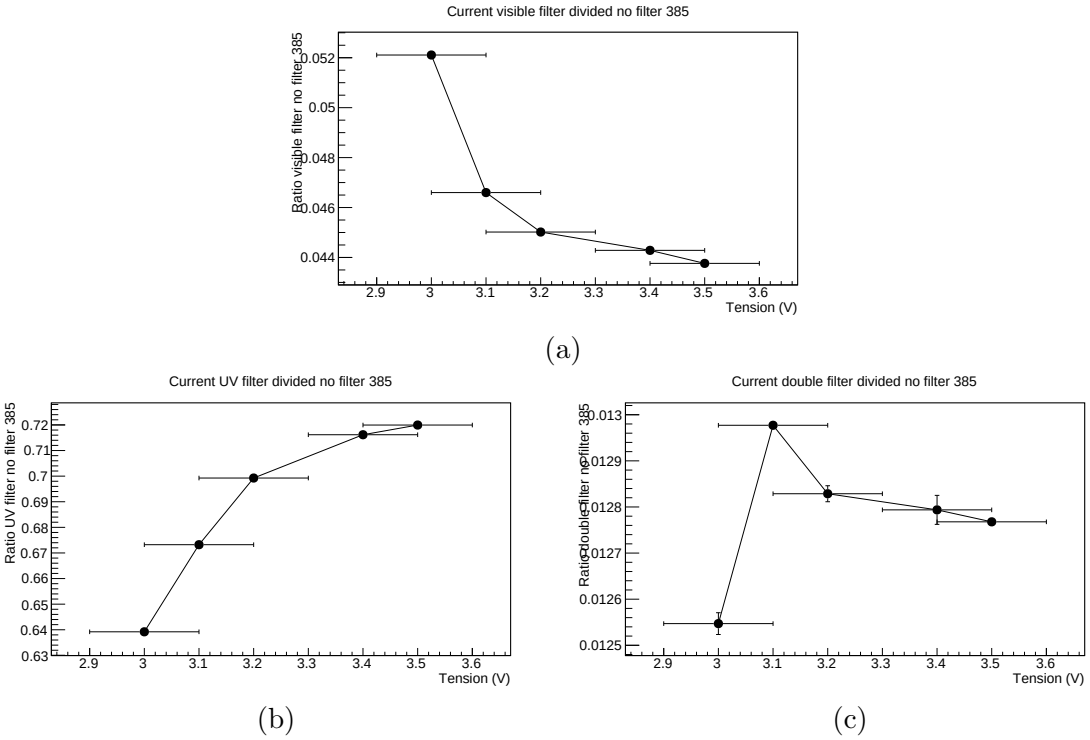

Figure 4.11: Ratio between the various combinations of the filters over no filter as function of the LED tension for 385 LED

Also in this case there is a decrease in the fraction of the visible light when the tension increases. At the same time, the fraction of UV light increases with the tension. The fact that the sum of the two components is not equal to 1 can be due to the fact that the relative positions of the LED, the filter and the pin-diode changed or the environment light changed. This could lead to a not so precise measurement of the fraction of the UV and visible light. In this case, there are no plateau since the current was limited to 30 mA and therefore also the voltage was limited.

For the RGB LED, data are taken only at one value of voltage that is the one that there will be during irradiation. The results are reported in Table

Filter	Green (A)	Blue (A)
No filter	$+3.7719 \cdot 10^{-06} \pm 1.2 \cdot 10^{-09}$	$1.16 \cdot 10^{-05} \pm 6 \cdot 10^{-07}$
Visible	$3.5672 \cdot 10^{-06} \pm 6 \cdot 10^{-10}$	$1.3329 \cdot 10^{-05} \pm 1.1 \cdot 10^{-08}$
UV	$+1.1590 \cdot 10^{-08} \pm 5 \cdot 10^{-12}$	$1.3404 \cdot 10^{-08} \pm 1.5 \cdot 10^{-11}$
Double	$+1.1297 \cdot 10^{-08} \pm 3 \cdot 10^{-12}$	$1.525 \cdot 10^{-08} \pm 1.5 \cdot 10^{-11}$

Table 4.3: Current for each filter combination for the Green and Blue LED

It's clear from the table that the assumption that the RGB has a negligible UV component is true since there are 2 order of magnitude of difference between the visible and the UV filters. From these data, the values of ϵ_{vis}^{vis} and ϵ_{vis}^{UV} can be found and are reported in the following table

	ϵ_{vis}^{vis}	ϵ_{vis}^{UV}
Blue	0.9652 ± 0.0013	$0.00116 \pm 6 \cdot 10^{-05}$
Green	0.9457 ± 0.0004	$0.003073 \pm 2 \cdot 10^{-06}$
Mean	0.9555 ± 0.0010	0.00212 ± 0.00010

Table 4.4: Values of the efficiencies for the RGB LED

From the table, it's clear that $\epsilon_{vis}^{vis} \approx 1$ and $\epsilon_{vis}^{UV} \approx 0$ as expected. The values of ϵ_{UV}^{vis}, ϵ_{UV}^{UV}, UV and vis are reported in the following table 4.5 (mean values of ϵ_{vis}^{vis} and ϵ_{vis}^{UV} were used).

	280	340	385
UV/L	0.8755	0.9854	0.9496
VIS/L	0.1246	0.01456	0.05041
ϵ_{UV}^{vis}	0.04357	0.008742	0.01732
ϵ_{UV}^{UV}	1.027	0.9413	0.7541

Table 4.5: Fraction of each component of the light, ϵ_{UV}^{vis} and ϵ_{UV}^{UV} for 280, 340 and 385 LEDs

For all the LEDs, ϵ_{UV}^{vis} is of the order of few percent while $\epsilon_{UV}^{UV} \approx 1$ for only the 280 and 340 LEDs. For the 385 there is a greater discrepancy. This can be due to the fact that 385 is near to the cut of the filter so there can be edge effect that spoil the measurement. Another explanation is that there could have been a modification in the relative position of the pin-diode, filter and LED when changing the filter.

4.5.3 Irradiation Results

As already explained, during the irradiation the light from the LEDs and at the end of the fiber was measured and also the environment light was measured. To avoid direct exposure to the γs, the two light distribution boxes and the power distribution circuit, were put inside a bunker made of lead bricks (see Fig 4.12)

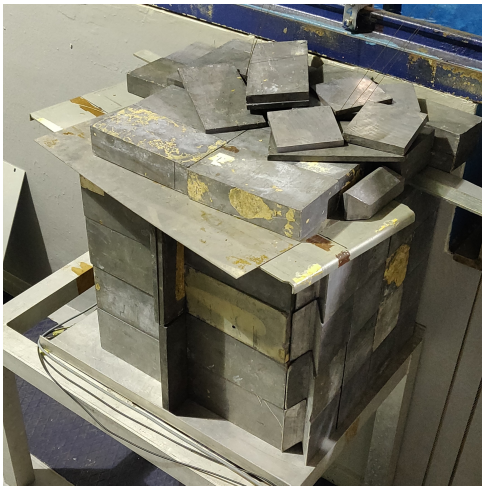

(a)

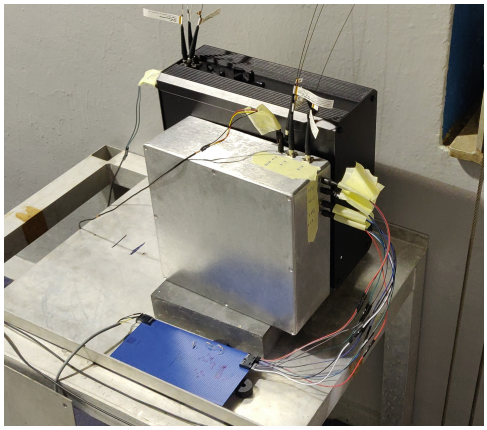

(b)

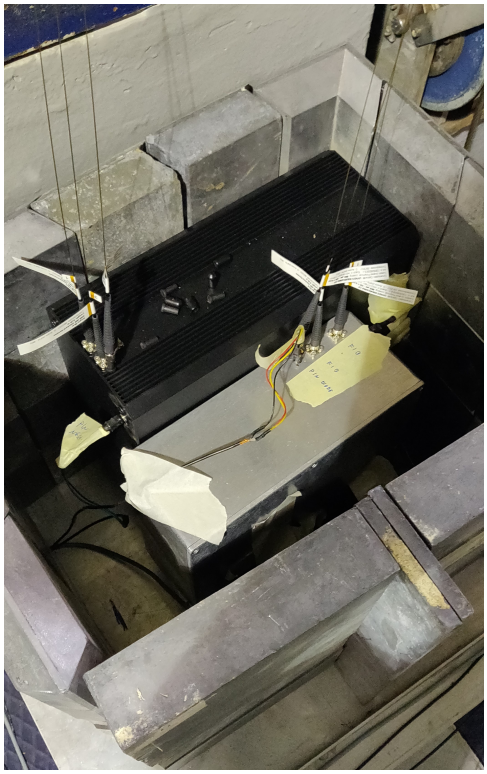

(c)

Figure 4.12: Photo of the bunker (a) where the two distribution boxes and the power distribution circuit were put during irradiation. Photo of the distribution boxes and the power distribution circuit before (b) and during (b) the building up of the bunker

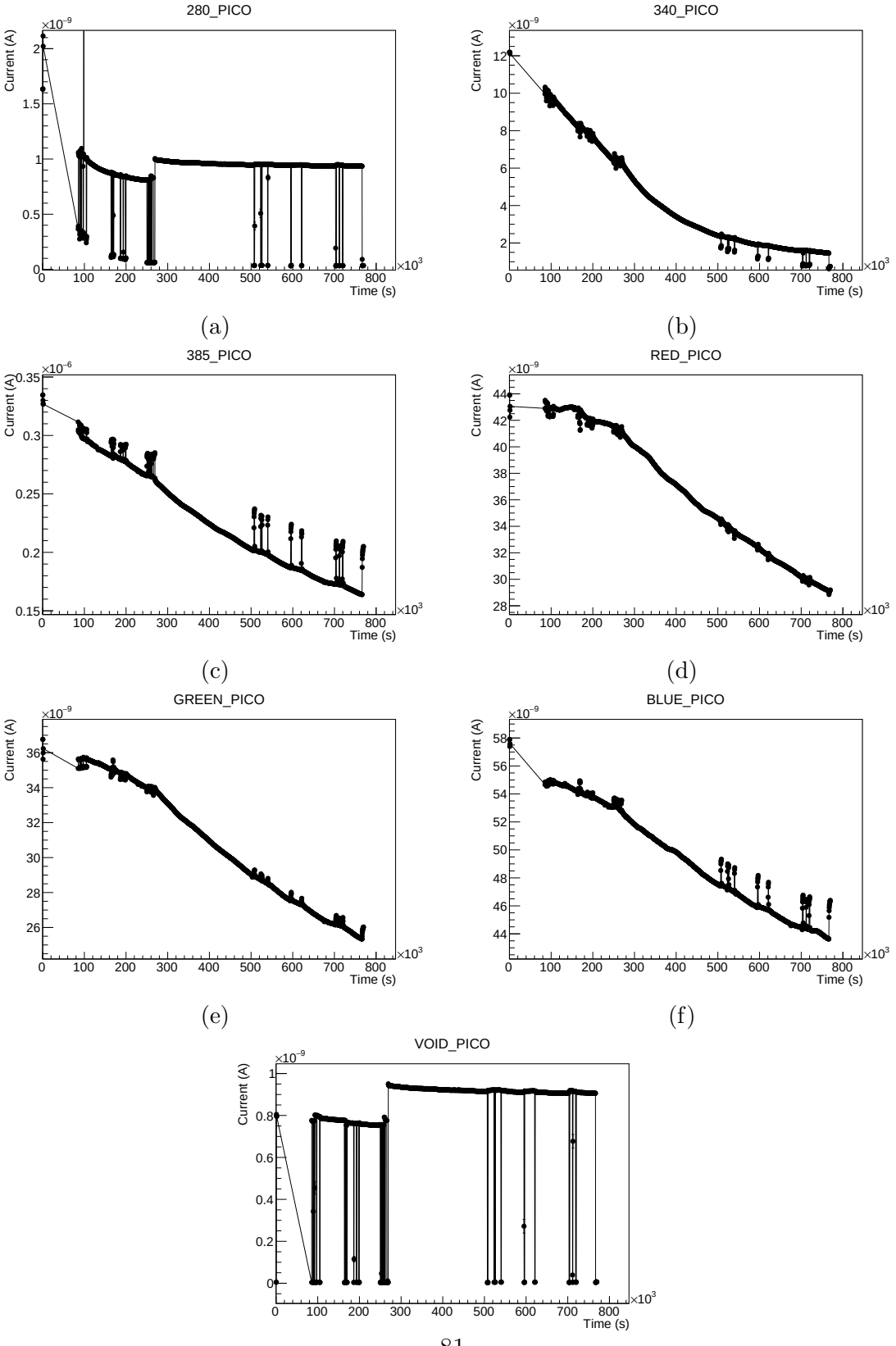

Figure 4.13: Light intensity as function of time at the end of the fiber

In Fig 4.13 there is a decrease in the light read by the fiber-pin-diode at the end of the fiber but this can be due to the LEDs instabilities. There is a gap at around $300 \cdot 10^3$ in the 280 and in the VOID. This gap is due to the change in the position of the fiber during the irradiation. It's clear that there is an effect on the fiber due to the γs. The spikes present in each graph corresponds to the moments where the source rack has been removed. Comparing the 280 with the VOID an issue rises: the signal coming from the 280 LED light is small compared with the background signal for almost all the irradiation. Therefore, after one single day almost all the light at $\lambda = 280$ has been lost. The hole at the start of the irradiation is due to a freeze of the PC.

In Fig 4.14 there is a decrease in time but is not so steep like in Fig 4.13. This means that part of the decrease is due to the irradiation. The spikes, like before are due to the presence/absence of the radioactive source. There is an oscillation in the light output of the red component of the RGB LED but it's small ($< 3\%$) and therefore is totally negligible. One of the possible cause is that the temperature of the LED changed, therefore also the current changes and the light output changes since it depends on the current.

To evaluate properly the light loss it's necessary first to subtract the background from the signals. After that, to eliminate the instabilities of the LED, a ratio between the picoammeter measurements and the sourcemeter ones is made. The results are reported in Fig 4.15.

For every LED, and therefore at every wavelength, there is a loss in the light transmission. For the 280 LED, the ratio at the start was ≈ 0.8 while at the end is ≈ 0.02 with a loss of signal of $\approx 97.5\%$ and almost all the loss happened in the first 24 hours. This could be a problem for the LUCID prototype since most of the Cherenkov light is in the UV region. Also in the region of 340 there is a huge loss, in fact at the start the ratio is ≈ 1.1 while at the end is ≈ 0.065 with a loss of 94%. In this case the loss is a little bit less than before but it could be a problem anyway. Contrary to the previous case, the loss is not concentrated in the first 24 hours but it is spread over all the irradiation time with a greater loss at the start. For the 385 LED the loss is smaller, in fact the ratio was ≈ 1.25 at the start of the irradiation and has diminished down to ≈ 0.73 with a loss of 41%. This is good for LUCID since the signal peak (the combination of the Cherenkov light spectrum with the quantum efficiency of the PMT) has its peak for wavelength between 340 and 385 nm. For the blue light, the ratio was ≈ 1.2 at the start of the irradiation and became ≈ 0.97 at the end of the irradiation with a loss of 19%. For the green light, the ratio passes from 1.82 to 1.32 with a loss of 27%. The green wavelength is not so interesting since the fraction of the blue and green light in the Cherenkov spectra is quite small. For wavelength near red, the ratio goes from 1.15 to 0.75 with a loss of 34%. This is the least interesting part of the spectrum for LUCID since it's outside the Cherenkov spectrum and PMT quantum efficiency.

As a general behavior, the UV light, and especially the deep UV light, shows a large transmission loss in a short time. Visible light and 385 nm light are affected to a lesser

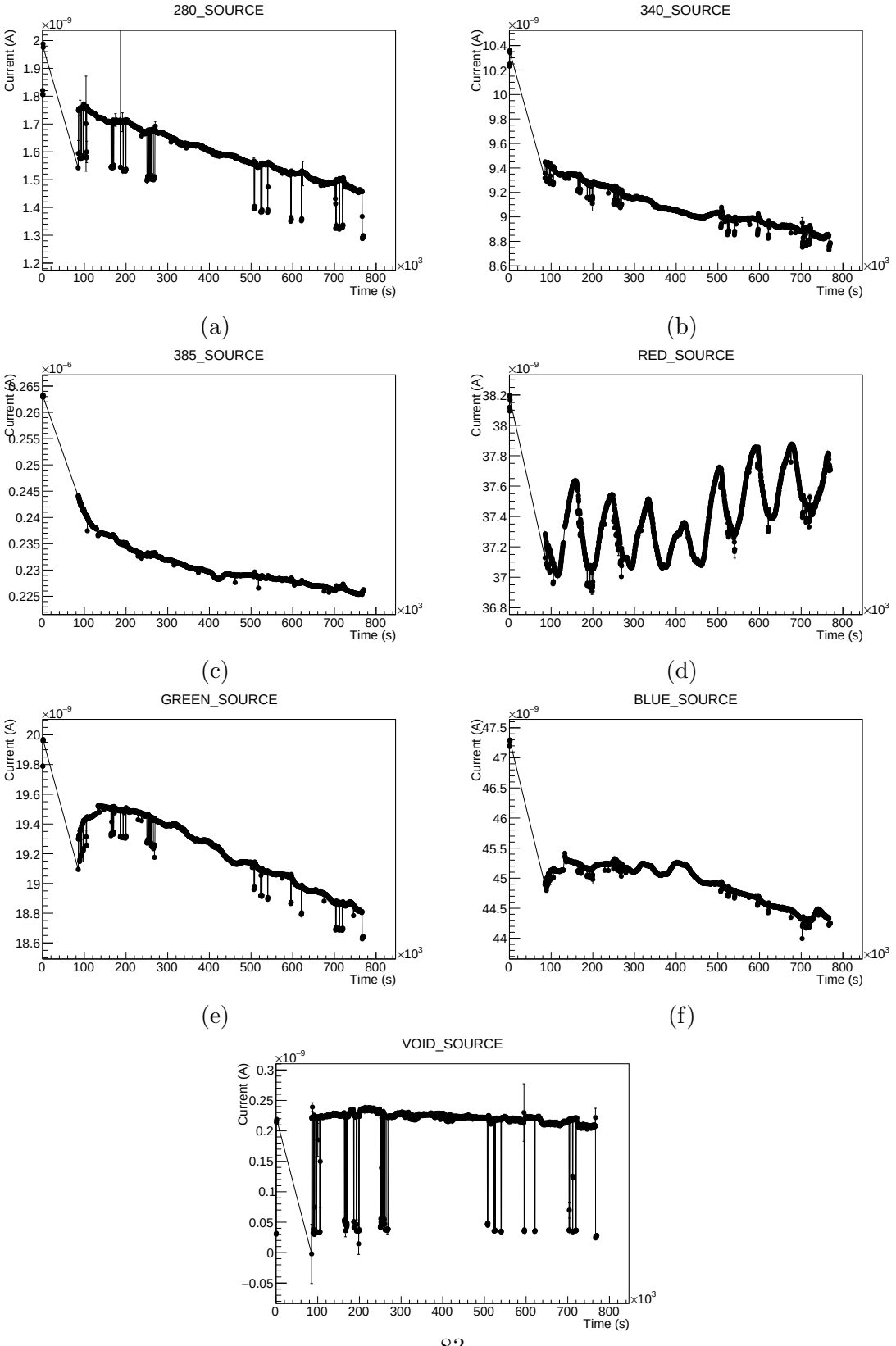

Figure 4.14: Light intensity as function of time at the start of the fiber

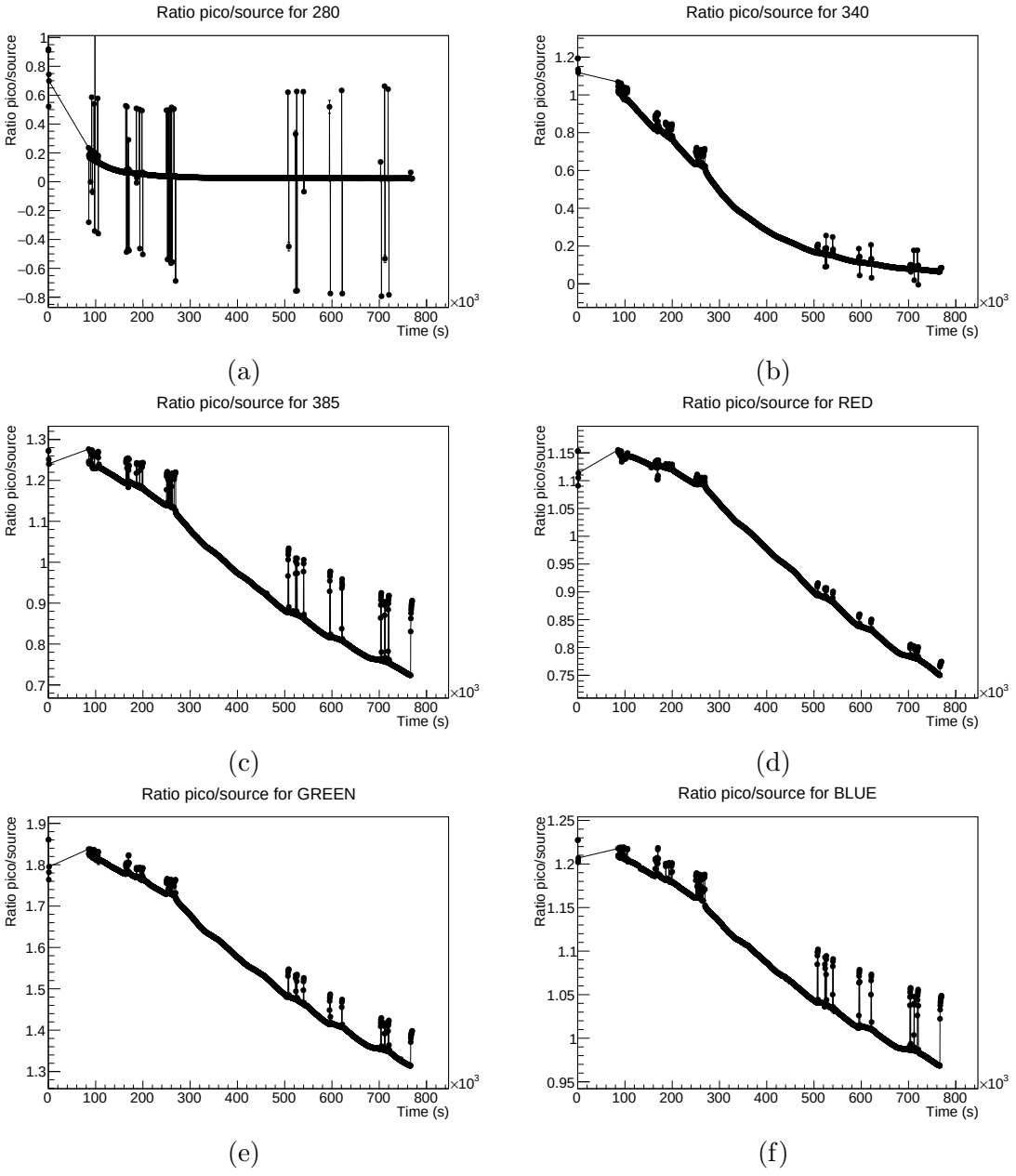

Figure 4.15: Ratio between the measurements of the picoammeter and sourcemeter

extent. Since UV light is the main component of the Cherenkov radiation, the fiber detector signal is expected to experience a drop in the first stages of data taking. The extent of the signal loss is to be determined using the data analyzed in this thesis together with detector and particle flow simulation.

Since 280 LED has a non-negligible component of visible light (see Tab 4.5) so it's necessary a more complicated analysis. To address this problem the λ for the BLUE LED was calculated via a fit. For the 280 is necessary a more complex fit model. It consists in a sum of two exponential that represent the visible and UV component of the light with respective ratio determined via Tab 4.5. The fit function is

$$ratio = ratio_0(UV \cdot e^{-\lambda_{UV} \cdot E} + (1 - UV) \cdot e^{-\lambda_{vis} \cdot E}) \tag{4.25}$$

where $ratio_0$ is the value of the ratio at the start of the irradiation and E is the energy absorbed by the fiber. λ_{VIS} has the same value of the BLUE light while the λ for the UV component is determined via the fit. Both fit are reported in Fig 4.16.

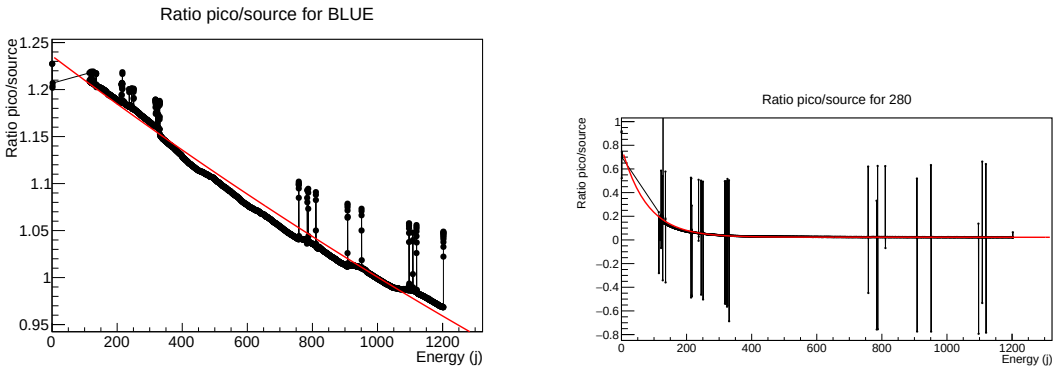

(a) (b)

Figure 4.16: Fit performed on the BLUE LED and 280 LED

From the fit of the BLUE LED, it is found that $\lambda_{BLUE} = 0.00021117 \pm 8 \cdot 10^{07}\ J^{-1}$. The result of the fit of 280 are reported in Table 4.6

$ratio_0$	λ_{UV}	λ_{vis}	UV
0.78 ± 0.05	0.0129 ± 0.0008	$4.4 \cdot 10^{-5} \pm 0.000450$	0.970 ± 0.010

Table 4.6: Results for the fit of the 280 LED

From this fit, the UV is found to be larger than what expected. This can be due to many factors like a systematic error in the previous test or a less-than perfect understanding of the fiber recovery. This, in combination with the fact that the loss for

the BLUE LED is almost linear, had led to a non-precise measurement of λ_{vis}. In fact, in this second fit, the uncertainty on λ_{vis} is greater than the value of λ_{vis} itself. This suggests that in the fit the best approximation for the ratio of visible light is a linear function, not an exponential.

Conclusions

The luminosity is a fundamental parameter for the LHC which is able to assess the performance of the collider. Moreover, the luminosity is related to cross section processes so its precise measurement is a fundamental part in the ATLAS physics program. LUCID-2, the ATLAS main luminometer during Run-2, was able to measure the luminosity with a precision of 1.7%. LUCID-2 is expected to satisfy all the requirements of the ATLAS physics program also for Run-3 but it won't be able to achieve the same task during HL-LHC for several reasons. First of all, the increase in the luminosity may cause the saturation of the algorithms in some lumiblocks and therefore the impossibility to measure the luminosity itself. Secondly, the precision in the luminosity measurement must reach 1% to cope with the ATLAS physics program. Therefore, a new detector must be built. Several detector projects have been made but they have to be tested. For this purpose, some prototypes will be installed and tested during Run-3. One of them is a fiber detector. For the correct operation of the detector it's important to understand how the fiber behaves when irradiated. For this purpose a session of γ irradiation was performed at the Calliope facility at ENEA. This irradiation session allows to study how the transmission of light inside the fiber is influenced when the fiber is irradiated. Using various LEDs, we have been able to study this effect as a function of the wavelength. For the deep UV region the loss is large ($\sim 95\%$) and can have a sizable impact on the luminosity measurement, for the region near 385 nm the loss is of the order of 41%. For the visible spectrum, the loss goes from 19% to 34%.

The results here reported suggest new studies. It's important to understand what happens if the light is not produced at the end of the fiber but in the middle. Another important factor that must be taken into account is the fact the particle flux in ATLAS is not constant along the fiber and the same is true for the direction of the Cherenkov light emission. These two effects must be evaluated via a GEANT4 simulation and then introduced as a correction factor in the calibration.

Bibliography

[1] S. White, *Determination of the absolute luminosity at the LHC*, 2010, http://cds.cern.ch/record/1308187.

[2] G. Cabras, *Luminosity determination for the mesurement of the proton-proton total cross-section at 8 TeV in the ATLAS experiment.*, PhD thesis, Università di Bologna, A.A. 2013/2014

[3] W. Herr, *Concept of Luminosity*, 2006, https://cds.cern.ch/record/941318, doi: 10.5170/CERN-2006-002.361

[4] S. Valentinetti, *Luminosity Measurements in ATLAS and CMS during Pp Data Taking at LHC*, in Proceedings of Sixth Annual Conference on Large Hadron Collider Physics, 2018, PoS LHCP2018, doi: 10.22323/1.321.0234

[5] H. Werner, *beam-beam interactions*, in Proceedings of CERN Accelerator School, 2006, doi: 10.5170/CERN-2006-002.379

[6] P. Grafström and W. Kozanecki, *Luminosity Determination at Proton Colliders.*, Prog. Part. Nucl. Phys. 81 (2015) 97, doi: 10.1016/j.ppnp.2014.11.002

[7] M. Aaboud *et al* (ATLAS Collaboration), *Luminosity Determination in pp Collisions at $\sqrt{s}$ = 8 TeV using the ATLAS Detector at the LHC*, Eur. Phys. J. C 76 (2016) 653.

[8] The ATLAS collaboration, *Luminosity determination in pp collisions at $\sqrt{s}$ = 13 TeV using the ATLAS detector at the LHC*, 2019, ATLAS-CONF-2019-021, https://cds.cern.ch/record/2677054

[9] S. van der Meer, *Calibration of the Effective Beam Height in the ISR*, CERN-ISR-PO-68-31, 1968, https://cds.cern.ch/record/296752

[10] K. Schindl, *The injector chain for the LHC*, in Proceedings of 9th LEP-SPS Performance Workshop, 1999, CERN-PS-99-018-DI, https://cds.cern.ch/record/384396

[11] G Aad *et al* (The ATLAS Collaboration), *The ATLAS Experiment at the CERN Large Hadron Collider*, Journal of Instrumentation 3 (2008) S08003.

[12] G. Avoni *et al*, *The New LUCID-2 Detector for Luminosity Measurement and Monitoring in ATLAS*, Journal of Instrumentation 13 (2018) P07017.

[13] P. Azzi *et al*, *Report from Working Group 1: Standard Model Physics at the HL-LHC and HE-LHC*, CERN Yellow Rep. Monogr. 7 (2019) 1.

[14] The ATLAS and CMS Collaborations, *Addendum to the report on the physics at the HL-LHC, and perspectives for the HE-LHC: Collection of notes from ATLAS and CMS*, CERN Yellow Rep.Monogr. 7 (2019) Addendum, doi: 10.23731/CYRM-2019-007.Addendum

[15] G. Aad *et al*, *Expected Performance of the ATLAS Experiment - Detector, Trigger and Physics*, 2009, arXiv: 0901.0512

[16] M. Aleska *et al.*, *ATLAS Phase-2 Upgrade: Phase-II Luminosity Task Force Report*, (2020), ATL-COM-UPGRADE-2020-012, https://cds.cern.ch/record/2714707

[17] The ATLAS Collaboration, *The LUCID 3 detector for the ATLAS Phase-II 2 Upgrade*, 2021, CERN-LHCC-2021-016, LHCC-P-018

[18] F. Attix, *Introduction to Radiological Physics and Radiation Dosimetry*, (1986), Wiley-VCH Verlag, ISBN: 9780471011460

[19] S. Baccaro and A. Cemmi, *Gamma irradiation Calliope facility at ENEA-Casaccia research centre (Rome, Italy)*, https://iris.enea.it/retrieve/handle/20.500.12079/6838/587/RT-2019-04-ENEA.pdf

[20] D. Jin, R. Connally, and J Piper, *Long-Lived Visible Luminescence of UV LEDs and Impact on LED Excited Time-Resolved Fluorescence Applications*, Journal of Physics 39 (2006) 461.